Available online at www.sciencedirect.com
ScienceDirect
Comput. Methods Appl. Mech. Engrg. 303 (2016) 260–287
Computer methods in applied mechanics and engineering
www.elsevier.com/locate/cma

A simple reduced integration hexahedral solid-shell element for large strains

Fernando G. Flores

IDIT-Departamento de Estructuras, Universidad Nacional de Córdoba y CONICET, Av. Velez Sarsfield 1611, 5016 Córdoba-Argentina, Argentina

Received 25 July 2015; received in revised form 12 November 2015; accepted 18 January 2016
Available online 12 February 2016

Abstract

In this paper a hexahedral solid-shell element with in-plane reduced integration is developed. The element is intended to the analysis of thin/thick elastic–plastic shells with moderate to large strains. Developed within the framework of a total Lagrangian formulation, the element uses as strain measure the logarithm of the right stretch tensor ($\mathbf{U}$) obtained from a modified right Cauchy–Green tensor ($\bar{\mathbf{C}}$). The modifications, in order to remove transverse shear, Poisson and volumetric locking, are three: (a) a classical assumed mixed shear strain approximation for C_{13} and C_{23} (b) an assumed strain approximation for the in-plane components $C_{\alpha\beta}$ and (c) an enhanced assumed strain for the through the thickness normal component C_{33} (one additional degree of freedom). The first five components of $\bar{\mathbf{C}}$ are interpolated to the integration points from values at the center of the top and bottom faces. An arbitrary number of integration points is used in the transverse direction and a stabilization scheme is used to avoid spurious modes due to the in-plane sub integration. Several examples are presented that show the locking-free behavior and the very good performance of the presented element for the analysis of shells with geometric and material nonlinearities, including quasi-incompressible elastic and elastic–plastic with incompressible plastic flow models.

Keywords: Finite elements; Solid-shell; Hexahedral; Large strains; Reduced integration; Stabilization

1. Introduction

The continuous improvement in computing facilities and the need to enhance various aspects of the models in order to achieve more faithful simulations has remarkably increased the use of solid elements for both structural analysis and industrial simulations. The main advantages of using solid elements are: (a) to consider truly three-dimensional constitutive relations not restricted to plane stress models; (b) a faithful treatment of boundary conditions in general and particularly the proper inclusion of contact forces on both faces, especially when friction is present; (c) to get rid of rotational degrees of freedom (DOFs) or local systems, which are generally computationally expensive and difficult to parameterize and update; (d) to deal with large transverse shear strains; and (e) to avoid special transition elements between solid and shell meshes.

E-mail address: fernando.flores@unc.edu.ar.

http://dx.doi.org/10.1016/j.cma.2016.01.013
0045-7825/

For strongly nonlinear problems, due for example to complex constitutive models or boundary conditions including contact, the simplest elements (linear interpolation) are preferred and, if possible, with only displacement (translational) DOFs. The solid-shell elements, i.e. when a single element through the thickness can be used, developed so far are mainly of hexahedral shape and a few are triangular prisms. Particularly where most of the developments have been made is on the trilinear 8-node element. It is well known that the standard displacement formulation for this element severely locks when modeling shells. These numerical lockings indicate the inability of the used interpolation functions (and their gradients) to conform to the shell behavior that often invalidate the solutions obtained. In bending problems transverse shear locking appears that increases with the slenderness of the shell. Also a linear interpolation of the displacement in the transverse direction does not allow that the transverse normal strain can fit a simple linear variation due to a non zero Poisson ratio, i.e. the normal transverse strain cannot accommodate the linear (bending) variation of the in-plane normal strains, leading to a locking behavior denoted by "Poisson effect". For initially curved shells membrane locking may appear for bending dominated problems without mid-surface stretching. Quasi-incompressible elastic constitutive models (associated to a Poisson ratio close to 0.5) or elastic–plastic materials with isochoric plastic flow introduce a constraint at each integration point leading to volumetric locking. Finally, a further locking effect observed is the so called trapezoidal locking. This effect is only found in structures where the out-of-plane edges are not normal to the mid-surface.

Furthermore, in order to have computationally efficient elements, it is necessary that the solid-shell element has a different integration scheme in the tangent plane of the shell (the minimum possible) than in the transverse direction, where the number of integration points must be arbitrary in order to be able to capture in detail the bending and the nonlinearities due to the constitutive model, particularly the elastic–plastic behavior. The use of a single point of integration in the plane of the shell requires, in order to maintain efficiency, the series expansion of different variables (e.g. the inverse Jacobian) and some control and/or stabilization of spurious deformation modes due to sub integration. The former implies some limitations on the allowable distortion of the elements and the latter usually leads to the introduction of factors that must be properly tuned. The advantages are however very large as these integration rules allow to markedly decrease the internal variables storage and CPU time, particularly in codes with explicit integration of the equations of motion.

Perhaps the first attempt to avoid hourglass problems is by Koslov and Frazier [1]. But the most important contributions to control hourglass of rank deficiency of underintegrated elements are due to Belytschko and coworkers for both solid and shell elements. They used perturbation stabilization [2], mixed methods [3], and assumed strain stabilization [4]. For shell elements based on the degenerated-solid approach Vu-Quoc and coworkers used perturbation method without user factors to filter spurious modes [5,6]. More recently, for reduced integration solid-shell elements, different stabilization schemes have been proposed that are highly dependent on the element formulation, see for example Refs. [7–12].

The developments made intended to curing the different locking behaviors mentioned above are numerous. A detailed state of the art on hexahedral solid-shell can be found in different Refs. [7,13,14,8]. A state of the art including all types of shell elements may be seen in [15]. To avoid locking due to a spurious increase of transverse shear stresses, Assumed Natural Strain (ANS) schemes are mainly used. The classical approach of Dvorkin and Bathe [16] is most considered when full integration is used in the plane of the shell (see for example the pioneering work of [17]), while for elements with reduced integration the scheme should be modified changing the location and increasing the sampling points, in order to avoid the appearance of spurious zero-strain modes (see for example [9]). In solid elements under large strains the volumetric locking has been solved using a mixed approach including constant pressure as originally proposed in [18]. The pressure DOF can be condensed at element level, averaging the volumetric strain and leading to an element with a constant volumetric strain. This technique is not acceptable for solid-shell elements because it leads to excessively flexible elements and does not allow a proper graduation of the transverse normal strain through the thickness. More recently Enhanced Assumed Strain (EAS [19]) techniques have been used, consisting of improving the deformation gradient or the strain tensor with the inclusion of internal DOFs that can be condensed at the element level maintaining displacements as the only global DOFs. The EAS technique can be used to eliminate the problems due to the Poisson effect, alleviate or eliminate the volumetric locking and can even be used to improve the membrane performance. This technique is not free of disadvantages, instabilities may appear, it may require a significant increase of the elemental database or to use an iterative loop at element level to determine the internal DOFs in each Newton–Raphson iteration. As shown in [11] and [9] use of a single internal DOF in combination with a reduced integration in the plane of the shell is enough to eliminate the locking due to the Poisson

effect and the volumetric locking. Alternatively, other authors [20,10,8] have included an additional translational DOF in the center of the element to improve the interpolation in the transverse direction. Also for use in composites (one element per layer), hybrid elements including transverse shear stress DOFs have been proposed that allows to satisfy the interlaminar stress continuity [21].

Most of the solid-shell elements in the literature are hexahedral (the middle surface is discretized with quadrilaterals). Only a few have a triangular base. In the author's knowledge the only triangular prism solid-shell elements are those proposed in [22,14] and [23]. The first two are limited to small elastic strains and only the third can deal with large strains. In this latter case the transverse shear locking is cured by means of a mixed assumed strain technique, while an EAS approach with a single additional DOF avoids the locking due to the Poisson effect. An assumed strain method for the in-plane components of the metric tensor, that resorts to the adjacent elements, avoids volumetric locking and also improves in-plane behavior. The integration rule used includes just one point in the triangle area and as many as desired across the thickness (two at least) without any stabilization needed. A key feature of this element is that 5 of the 6 different components of the right Cauchy–Green deformation tensor are calculated on the external surfaces (top and bottom) of the element and are linearly interpolated across the thickness. As the right Cauchy–Green tensor $\mathbf{C}$ is interpolated across the element, a Total Lagrangian Formulation with any strain measure derived from $\mathbf{C}$ is the natural choice. In particular for small strains the Green–Lagrange strain can be used and for moderate to large strains the material logarithmic strain is a suitable choice. Both isotropic and orthotropic hyperelastic materials can be easily implemented, and also orthotropic elastic–plastic materials can be considered. This paper proposes to extend the ideas used in the formulation of the 6-node "prism" element [23] to an 8-node hexahedral element. In this case one in-plane integration point requires hourglass stabilization. The approach here is based on the decomposition of the ANS interpolation into the strains computed along the element axis plus their differences denoted here as stabilization strains. These stabilization strains lead to the definition of an internal strain energy that is computed, disregarding some terms, in a simplified form. Note that the so defined stabilization strains are locking free as long as the ANS formulation is locking free.

In the next section the basic formulation of the solid element is summarized. Then the improvements in the standard element are presented, detailing the necessary expressions for the computation of the tangent matrix and the stabilization scheme. Initially the assumed strain technique for the in-plane components is developed, then the formulation of the transverse shear and finally the EAS technique used to prevent locking due to the Poisson effect is presented. Section 4 presents several examples showing the very good performance of the element and finally some conclusions are summarized.

2. Formulation of the basic solid finite element

The reference and deformed geometries of the hexahedral element are described by the standard isoparametric approximations [24].

$$\mathbf{X}(\boldsymbol{\xi}) = \sum_{I=1}^{8} N^I(\boldsymbol{\xi})\,\mathbf{X}^I \tag{1}$$

$$\mathbf{x}(\boldsymbol{\xi}) = \sum_{I=1}^{8} N^I(\boldsymbol{\xi})\,\mathbf{x}^I = \sum_{I=1}^{8} N^I(\boldsymbol{\xi})\left(\mathbf{X}^I + \mathbf{u}^I\right) \tag{2}$$

where $\mathbf{X}^I$, $\mathbf{x}^I$, and $\mathbf{u}^I$ are the original coordinates, present coordinates and displacements respectively of node I. The shape functions $N^I(\xi)$ are the usual trilinear Lagrangian polynomials in terms of the local coordinates $\boldsymbol{\xi}$ of the master element, where (ξ, η) are associated with the middle surface and ζ with the transverse direction:

$$N^I(\xi,\eta,\zeta) = \frac{1}{4}\left(1+\xi^I\xi\right)\left(1+\eta^I\eta\right)\frac{1}{2}\left(1+\zeta^I\zeta\right). \tag{3}$$

Above $\left(\xi^I, \eta^I, \zeta^I\right)$ are the natural coordinates of node I. These shape functions can also be written as the product of the bilinear interpolation functions on each external face (lower and upper) and the linear interpolation functions in the transverse direction

$$N^L(\xi,\eta,\zeta) = \frac{1}{4}\left(1+\xi^L\xi\right)\left(1+\eta^I\eta\right)L^1(\zeta) \quad L = 1,4$$

$$N^U(\xi,\eta,\zeta) = \frac{1}{4}\left(1+\xi^U\xi\right)\left(1+\eta^U\eta\right)L^2(\zeta) \quad U = 5,8 \tag{4}$$

$$L^1 = \frac{1}{2}(1-\zeta) \qquad L^2 = \frac{1}{2}(1+\zeta)\,. \tag{5}$$

At the element center a local Cartesian system can be defined:

$$\mathbf{R}^C = \left[\mathbf{t}_1^C, \mathbf{t}_2^C, \mathbf{t}_3^C\right] \tag{6}$$

with the first two axes ($\mathbf{t}_1^C$ and $\mathbf{t}_2^C$) on the tangent plane to the middle surface, that can be associated with the principal orthotropic directions (elastic or plastic) of the constitutive material or other convenient condition. Defining the Jacobian matrix at any point of interest

$$\mathbf{J} = \frac{\partial \mathbf{X}}{\partial \boldsymbol{\xi}} \tag{7}$$

the computation of the Cartesian derivatives with respect to the global system is in a standard way

$$N^I_{\mathbf{X}} = \mathbf{J}^{-1}\, N^I_{\boldsymbol{\xi}} \tag{8}$$

while the Cartesian derivatives with respect to the local system ($\mathbf{Y}$) are

$$N^I_{\mathbf{Y}} = \mathbf{R}^T\, N^I_{\mathbf{X}} \tag{9}$$

where the local transformation matrix $\mathbf{R}$ must be defined at each point in terms of (6). These derivatives allow to compute the deformation gradient $\mathbf{F}$ in terms of the present nodal coordinates as

$$F_{ij} = \sum_{I=1}^{8} N^I_{y_j}\, x^I_i \tag{10}$$

so that the components of the right Cauchy–Green deformation tensor $\mathbf{C}$ refereed to the local system are

$$C_{ij} = F_{ki}\,F_{kj}\,. \tag{11}$$

Tensor $\mathbf{C}$ allows to compute different Lagrangian (material) strain measures, in particular: the Green–Lagrange strain tensor

$$\mathbf{E} = \frac{1}{2}(\mathbf{C} - \mathbf{1}) \tag{12}$$

suitable for elastic problems in small strains and the logarithmic strain tensor

$$\mathbf{e} = \ln \mathbf{C}^{1/2} \tag{13}$$

that can be used for elastic–plastic models in metals under moderate to large strains. In the Refs. [25,23] several examples with such an approach can be found in plane stress and three dimensional models.

As shown in the next section the tensor $\mathbf{C}$ is modified using assumed strain techniques that in one case involve an internal DOF α, leading to an enhanced tensor $\bar{\mathbf{C}}$. The balance equations to be solved (variational formulation) are for the large deformation case

$$g_1(\mathbf{u},\alpha) = \int_{V_o} \frac{1}{2}\mathbf{S}\left(\bar{\mathbf{C}}\right) : \delta_{\mathbf{u}}\bar{\mathbf{C}}\, dV_0 + g_{ext} = 0 \tag{14}$$

$$g_2(\mathbf{u},\alpha) = \int_{V_o} \frac{1}{2}\mathbf{S}\left(\bar{\mathbf{C}}\right) : \delta_{\alpha}\bar{\mathbf{C}}\, dV_0 = 0 \tag{15}$$

where $\mathbf{S}$ is the second Piola–Kirchhoff stress tensor and g_{ext} is the virtual work of the external forces.

3. Improvements in the element

To use the above hexahedral element in problems involving shells with large strain elastic–plastic models including contact conditions, its behavior must be substantially improved. The proposed modifications are made directly on the components of the right Cauchy–Green tensor.

The discretization of a shell with 8-node solid elements usually implies two steps: (a) a discretization of the middle surface with 4-node quadrilaterals and (b) a discretization of the shell thickness with one or more solid elements based on each quadrilateral on the middle surface. It will then be assumed that, as it was already established at Eq. (4), that the 8-node element connectivities associate the local nodes 1–4 and 5–8 with surfaces at similar distances of the middle surface, and that the last four nodes are above the first four nodes at a distance along the shell normal equal to the shell thickness or a layer thickness. In this way the normal direction to the middle surface (local y_3 coordinate) is parallel or almost parallel to the local natural coordinate ζ. This assumption about the finite element mesh precludes the existence of the so-called trapezoidal locking. For the purpose of having an element as simple and efficient as possible, no cure for this type of locking is attempted, therefore its use should not be extended to models where external surfaces discretizations are not made under the conditions stated.

The equations to be solved ((14)–(15)) have been written in terms of the right Cauchy–Green tensor, then a straightforward possibility is to propose modifications on the components of $\mathbf{C}$ that are directly involved in the behavior to improve. Distinguishing

$$\mathbf{C} = \begin{bmatrix} C^m_{11} & C^m_{12} & C^s_{13} \\ C^m_{21} & C^m_{22} & C^s_{23} \\ C^s_{31} & C^s_{32} & C^t_{33} \end{bmatrix}. \tag{16}$$

In the above expression the superscript m indicates components with the largest influence on the shell in-plane behavior (membrane and bending), while the superscript s refers to those that have a direct influence on the transverse shear and the index t is associated with transverse normal component which has its main influence on the normal strain across the thickness. The tensor $\mathbf{C}$ then can be decomposed into three parts

$$\mathbf{C} = \mathbf{C}^m + \mathbf{C}^s + \mathbf{C}^t \tag{17}$$

with

$$\begin{aligned} \mathbf{C}^m &= C_{11}\mathbf{t}^1 \otimes \mathbf{t}^1 + C_{22}\mathbf{t}^2 \otimes \mathbf{t}^2 + C_{12}\left(\mathbf{t}^1 \otimes \mathbf{t}^2 + \mathbf{t}^2 \otimes \mathbf{t}^1\right) \\ \mathbf{C}^s &= C_{13}\left(\mathbf{t}^1 \otimes \mathbf{t}^3 + \mathbf{t}^3 \otimes \mathbf{t}^1\right) + C_{23}\left(\mathbf{t}^2 \otimes \mathbf{t}^3 + \mathbf{t}^3 \otimes \mathbf{t}^2\right) \\ \mathbf{C}^t &= C_{33}\mathbf{t}^3 \otimes \mathbf{t}^3. \end{aligned} \tag{18}$$

The modifications introduced on each part of $\mathbf{C}$ are developed in the sequel. The approach proposed for $\mathbf{C}^m$ is similar to that introduced in [26] for the computation of the first fundamental form in a rotation-free shell element. The modification on $\mathbf{C}^s$ is an assumed mixed interpolation of tensorial components based on the approximation initially proposed in [16] and is similar to that described in [27] but modifying the sampling points as suggested in [9]. Finally for $\mathbf{C}^t$ a modified EAS technique with one additional DOF [11,9] is considered. Note that the modification on $\mathbf{C}$ can naturally be seen as modifications on the Green–Lagrange strain tensor $\mathbf{E}$ due to the linear relation between them. Besides that, the spectral decomposition of the right Cauchy–Green tensor can be used for the evaluation of different strain measures and directly in different hyperelastic constitutive models.

Remind that in contrast with a hexahedral solid element where the usual integration scheme is $2 \times 2 \times 2$, for the shell elements the number of integration points in the transverse direction is arbitrary (minimum 2 but may be as large as 21), while in the plane of the shell a reduced integration 1×1 is usually sought plus a stabilization scheme. The integration rule will lead, due to optimization reasons, to a particular evaluation of the equivalent nodal forces and the geometric stiffness matrix. For the volume integration, the Jacobian of the isoparametric approach is computed at three points, namely the element center and the center of the upper and lower surfaces. This three values are quadratically interpolated to the integration points for an accurate computation of the element volume for initially curved geometries.

3.1. Membrane/bending components

First remind that at each external face the position of the 4-node surface results from the usual bi-linear interpolation obtained from (4) as particular cases:

$$\mathbf{X}^L(\xi,\eta) = \sum_{I=1}^{4} N^I(\xi,\eta,\zeta=-1)\ \mathbf{X}^I \tag{19}$$

$$\mathbf{X}^U(\xi,\eta) = \sum_{I=5}^{8} N^I(\xi,\eta,\zeta=+1)\ \mathbf{X}^I \tag{20}$$

where $\mathbf{X}^L$ and $\mathbf{X}^U$ are the position of the lower and upper faces respectively.

In the approximation defined next, the components of $\bar{\mathbf{C}}^m$ on the shell tangent plane are written as a function of values $\bar{C}^f_{\alpha\beta}$ $(\alpha,\beta=1,2)$ associated with the center of the lower $(L,\ f=1)$ and upper $(U,\ f=2)$ faces. These values are linearly interpolated to the n_G integration point across the thickness using

$$\bar{C}_{\alpha\beta}(\zeta) = L^1(\zeta)\,\bar{C}^1_{\alpha\beta} + L^2(\zeta)\,\bar{C}^2_{\alpha\beta}. \tag{21}$$

For the computation of $\bar{C}^f_{\alpha\beta}$ we resort to the same strategy proposed in [26].

The computation of $\bar{\mathbf{C}}^m$ at each face to replace the standard approximation requires a definition of the local Cartesian system $\mathbf{R}$ consistent with $\mathbf{R}^C$ (Eq. (6)) at each point where the gradient $\frac{\partial \mathbf{X}}{\partial \boldsymbol{\xi}} \equiv \mathbf{X}_{\boldsymbol{\xi}}$ is computed. For that aim it is proposed:

(a) At each mid-side point K of face f the tangent plane $(\mathbf{X}^K_\xi, \mathbf{X}^K_\eta)$ and its normal $\mathbf{t}^K$ are computed with

$$\mathbf{t}^K = \frac{\left(\mathbf{X}^K_\xi \times \mathbf{X}^K_\eta\right)}{\left\|\mathbf{X}^K_\xi \times \mathbf{X}^K_\eta\right\|} = \frac{\left(\mathbf{X}^K_\xi \times \mathbf{X}^K_\eta\right)}{J_K} \tag{22}$$

where J_K is the Jacobian determinant of the isoparametric mapping in the original configuration.

(b) The continuity with the Cartesian system $\mathbf{R}^C$ is achieved using the intersection $\mathbf{q}^K$ between the plane $\left(\mathbf{t}^C_1, \mathbf{t}^C_2\right)$ and the tangent plane at point K: $\mathbf{q}^K = \frac{\mathbf{t}^C_3 \times \mathbf{t}^K}{\left\|\mathbf{t}^C_3 \times \mathbf{t}^K\right\|}$ and the angle α between $\mathbf{q}^K$ and the in-plane reference directions $\cos\alpha = \mathbf{q}^K \cdot \mathbf{t}^C_1$ and $\sin\alpha = \mathbf{q}^K \cdot \mathbf{t}^C_2$. Finally the directions $(\mathbf{t}^K_1, \mathbf{t}^K_2)$ are chosen on the plane $(\mathbf{X}^K_\xi, \mathbf{X}^K_\eta)$ such that the same angle α is obtained with $\mathbf{q}^K$ $(\mathbf{q}^K \cdot \mathbf{t}^K_1 = \cos\alpha$ and $\mathbf{q}^K \cdot \mathbf{t}^K_2 = \sin\alpha)$.

(c) Once $(\mathbf{t}^K_1, \mathbf{t}^K_2)$ are defined, the local in-plane Jacobian matrix is

$$\mathbf{J}_K = \begin{bmatrix} \mathbf{X}^K_\xi \cdot \mathbf{t}^K_1 & \mathbf{X}^K_\eta \cdot \mathbf{t}^K_1 \\ \mathbf{X}^K_\xi \cdot \mathbf{t}^K_2 & \mathbf{X}^K_\eta \cdot \mathbf{t}^K_2 \end{bmatrix}. \tag{23}$$

(d) That allows to obtain: the shape function derivatives, that involve only the four nodes of each face,

$$\begin{bmatrix} N^I_1 \\ N^I_2 \end{bmatrix}^K = \mathbf{J}^{-1}_K \begin{bmatrix} N^I_\xi \\ N^I_\eta \end{bmatrix}^K, \tag{24}$$

the deformation gradient on the tangent plane in the deformed configuration $(\mathbf{f}^K_1, \mathbf{f}^K_2)$ and with it $C^K_{\alpha\beta}$.

These Cartesian in-plane components of the right Cauchy–Green tensor can be used in an assumed strain approach interpolating them to the integration points. A reduced integration is proposed for the present element, then those components are simple weighted averaged over each face $\bar{C}^f_{\alpha\beta}$

$$\bar{C}^f_{a\beta} = \frac{1}{A^f} \sum_{K=1}^{4} J_K\ C^K_{\alpha\beta} \qquad \sum_{K=1}^{4} J_K = A^f. \tag{25}$$

Note that the script K indicates values at point K of face f but to avoid too many scripts only the index K is kept in the notation.

The components of the Green–Lagrange strain tensor on each face center may be written as

$$\bar{E}^f_{\alpha\beta} = \frac{1}{2}\frac{1}{A^f}\sum_{K=1}^{4} J_K \left[C^K_{\alpha\beta} - \delta_{\alpha\beta}\right] = \frac{1}{2}\left(\bar{C}^f_{\alpha\beta} - \delta_{\alpha\beta}\right) \tag{26}$$

with $\delta_{\alpha\beta}$ the Kronecker delta.

The associated tangent matrix $\bar{\mathbf{B}}_m$ relating displacement increments $\delta\mathbf{u}$ with changes in the in-plane components of the tensor is the sum:

$$\delta\begin{bmatrix} \frac{1}{2}\bar{C}_{11} \\ \frac{1}{2}\bar{C}_{22} \\ \bar{C}_{12} \end{bmatrix} = L^1\delta\begin{bmatrix} \frac{1}{2}\bar{C}^1_{11} \\ \frac{1}{2}\bar{C}^1_{22} \\ \bar{C}^1_{12} \end{bmatrix} + L^2\begin{bmatrix} \frac{1}{2}\bar{C}^2_{11} \\ \frac{1}{2}\bar{C}^2_{22} \\ \bar{C}^2_{12} \end{bmatrix} = \delta\begin{bmatrix} E_{11} \\ E_{22} \\ 2E_{12} \end{bmatrix} \tag{27}$$

where each term is

$$\begin{aligned} \delta\begin{bmatrix} \frac{1}{2}\bar{C}^f_{11} \\ \frac{1}{2}\bar{C}^f_{22} \\ \bar{C}^f_{12} \end{bmatrix} &= \bar{\mathbf{B}}^f_m\delta\mathbf{u}^f = \frac{1}{A^f}\sum_{K=1}^{4} J_K\,\delta\begin{bmatrix} \frac{1}{2}C^K_{11} \\ \frac{1}{2}C^K_{22} \\ C^K_{12} \end{bmatrix} \\ &= \frac{1}{A^f}\sum_{K=1}^{4} J_K \sum_{J=1}^{4}\begin{bmatrix} \mathbf{f}^K_1 N^J_1 \\ \mathbf{f}^K_2 N^J_2 \\ \left(\mathbf{f}^K_1 N^J_2 + \mathbf{f}^K_2 N^J_1\right) \end{bmatrix}\delta\mathbf{u}^K. \end{aligned} \tag{28}$$

Note that the vector $\delta\mathbf{u}^f$ includes only the nodes of the face f (lower or upper). Then it is possible to write

$$\left[\bar{\mathbf{B}}_m\right]_{3\times 24} = \left[L^1\bar{\mathbf{B}}^1_m \quad L^2\bar{\mathbf{B}}^2_m\right] \tag{29}$$

where each matrix on the right hand side is associated with a different set of nodes, as matrix $\bar{\mathbf{B}}^1_m$ is associated with the nodes in the lower face and $\bar{\mathbf{B}}^2_m$ with the nodes in the upper face only.

The equivalent nodal force vector $\delta\mathbf{u}^T\mathbf{r}_m$ stems from the integral

$$\begin{aligned} \delta\mathbf{u}^T\int_{-1}^{1}\begin{bmatrix} S_{11} \\ S_{22} \\ S_{12} \end{bmatrix}^T\left[L^1\bar{\mathbf{B}}^1_m, \quad L^2\bar{\mathbf{B}}^2_m\right]J d\zeta &= \delta\mathbf{u}^T\left\{\int_{-1}^{1}\begin{bmatrix} S_{11} \\ S_{22} \\ S_{12} \end{bmatrix}^T L^1 J d\zeta\,\bar{\mathbf{B}}^1_m, \int_{-1}^{1}\begin{bmatrix} S_{11} \\ S_{22} \\ S_{12} \end{bmatrix}^T L^2 J d\zeta\,\bar{\mathbf{B}}^2_m\right\} \\ &= \delta\mathbf{u}^T\left\{\begin{bmatrix} \bar{S}^1_{11} \\ \bar{S}^1_{22} \\ \bar{S}^1_{12} \end{bmatrix}^T\bar{\mathbf{B}}^1_m, \begin{bmatrix} \bar{S}^2_{11} \\ \bar{S}^2_{22} \\ \bar{S}^2_{12} \end{bmatrix}^T\bar{\mathbf{B}}^2_m\right\} \end{aligned} \tag{30}$$

where

$$\delta\mathbf{u}^T = \left[\delta\mathbf{u}^T_1\,\delta\mathbf{u}^T_2\,\delta\mathbf{u}^T_3\,\delta\mathbf{u}^T_4\,\delta\mathbf{u}^T_5\,\delta\mathbf{u}^T_6\,\delta\mathbf{u}^T_7\,\delta\mathbf{u}^T_8\right] \tag{31}$$

and

$$\bar{\mathbf{S}}^f = \begin{bmatrix} \bar{S}^f_{11} \\ \bar{S}^f_{22} \\ \bar{S}^f_{12} \end{bmatrix} = \int_{-1}^{1}\begin{bmatrix} S_{11} \\ S_{22} \\ S_{12} \end{bmatrix} L^f\,J\,d\zeta. \tag{32}$$

3.1.1. Geometric stiffness matrix

The geometric stiffness matrix $\delta\mathbf{u}^T\mathbf{K}_m^G\Delta\mathbf{u}$ results from the derivative:

$$\int_V \frac{\partial}{\partial\mathbf{u}}\left(\delta\begin{bmatrix}\frac{1}{2}\bar{C}_{11}\\ \frac{1}{2}\bar{C}_{22}\\ \bar{C}_{12}\end{bmatrix}\right)^T\begin{bmatrix}S_{11}\\ S_{22}\\ S_{12}\end{bmatrix}\Delta\mathbf{u}\,dV \tag{33}$$

replacing Eq. (28) it can be written as:

$$\sum_{G=1}^{n_G} V_G \sum_{f=1}^{2}\frac{L^f}{A^f}\sum_{K=1}^{4} J_K \sum_{I=1}^{4}\sum_{J=1}^{4}\left\{\delta\mathbf{u}^I\begin{bmatrix}N_1^I N_2^I\end{bmatrix}\begin{bmatrix}S_{11} & S_{12}\\ S_{21} & S_{22}\end{bmatrix}\begin{bmatrix}N_1^J\\ N_2^J\end{bmatrix}\Delta\mathbf{u}^J\right\} \tag{34}$$

where the sum on G is the numerical integration with n_G points in ζ direction. The values $\bar{\mathbf{S}}^f$ computed above (Eq. (32)) can be advantageously used rearranging the different sums

$$\begin{aligned}&\sum_{f=1}^{2}\sum_{K=1}^{4}\frac{J_K}{A^f}\sum_{I=1}^{4}\sum_{J=1}^{4}\left\{\delta\mathbf{u}^I\begin{bmatrix}N_1^I N_2^I\end{bmatrix}\left[\sum_{G=1}^{n_G} V_G L^f\begin{bmatrix}S_{11} & S_{12}\\ S_{21} & S_{22}\end{bmatrix}\right]\begin{bmatrix}N_1^J\\ N_2^J\end{bmatrix}\Delta\mathbf{u}^J\right\}\\ &\quad=\sum_{f=1}^{2}\left\{\sum_{K=1}^{4}\frac{J_K}{A^f}\sum_{I=1}^{4}\sum_{J=1}^{4}\delta\mathbf{u}^I\begin{bmatrix}N_1^I N_2^I\end{bmatrix}\begin{bmatrix}\bar{S}_{11}^f & \bar{S}_{12}^f\\ \bar{S}_{21}^f & \bar{S}_{22}^f\end{bmatrix}\begin{bmatrix}N_1^J\\ N_2^J\end{bmatrix}\Delta\mathbf{u}^J\right\}^f\end{aligned} \tag{35}$$

where again the contributions of each face are independent one from the other.

3.1.2. Membrane stabilization

The one-point integration rule in the shell plane requires some sort of stabilization to avoid the appearance of spurious zero-energy deformation modes (*hourglass*). For that purpose stabilization Green–Lagrange strains (ε) are defined at each mid-side point K of each face f as the difference between the metric tensor at those points and the weighted average at the face center,

$$\varepsilon_{\alpha\beta}^K = \frac{1}{2}\left(C_{\alpha\beta}^K - \bar{C}_{a\beta}^f\right). \tag{36}$$

Note also that at each face f:

$$\sum_{K=1}^{4} J_K\varepsilon_{\alpha\beta}^K = \frac{1}{2}\sum_{K=1}^{4} J_K C_{\alpha\beta}^K - \frac{1}{2}A^f\bar{C}_{a\beta}^f = 0. \tag{37}$$

The variation of these strains is

$$\begin{aligned}\delta\varepsilon_{\alpha\beta}^K &= \left(N_{,\alpha}^I\mathbf{x}_{,\beta} + N_{,\beta}^I\mathbf{x}_{,\alpha}\right)^K\cdot\delta\mathbf{u}^I - \frac{1}{A^f}\sum_{J=1}^{4} J_i\left(N_{,\alpha}^I\mathbf{x}_{,\beta} + N_{,\beta}^I\mathbf{x}_{,\alpha}\right)^J\cdot\delta\mathbf{u}^I\\ &= \mathbf{B}_m^{KH}\,\delta\mathbf{u}^e = \left[\mathbf{B}_m^K - \bar{\mathbf{B}}_m^f\right]\delta\mathbf{u}^e\end{aligned} \tag{38}$$

note also that $\mathbf{B}_m^{KH}$ is just the difference $\mathbf{B}_m^K - \bar{\mathbf{B}}_m^f$, therefore the additional computational cost of the membrane stabilization is quite low. The associated strain energy can be written for stabilization purposes (β_m is a factor less that 1) as

$$W_m^H = \frac{1}{2}\beta_m E 8 J_0\sum_{f=1}^{2}\sum_{K=1}^{4}\frac{J_K}{A^f}\left\{\left(\varepsilon_{11}^K\right)^2 + \left(\varepsilon_{22}^K\right)^2 + \frac{1}{2}\left(2\varepsilon_{12}^K\right)^2\right\}^f \tag{39}$$

based on geometrical considerations it can be seen that any hourglass mode must lead to a non-zero shear strain at mid-side points, so to decrease the computational cost even more, only the cross term ε_{12}^{K} is kept, reducing the stabilization strain energy to just:

$$W_m^H = \frac{1}{2}\beta_m E4J_0 \sum_{f=1}^{2}\sum_{K=1}^{4} \frac{J_K}{A^f}\left(2\varepsilon_{12}^{K}\right)^2. \tag{40}$$

Defining stabilization forces at each mid-side point of each face

$$\sigma_{12}^{K} = \beta_m E4J_0 \frac{J_K}{A^f} 2\varepsilon_{12}^{K} \tag{41}$$

the stabilization nodal forces result

$$\mathbf{r}_m^H = \sum_{f=1}^{2}\sum_{K=1}^{4} \sigma_{12}^{K}\left(\mathbf{B}_m^{KH}\right)_{12} \tag{42}$$

while the contribution to the elemental stiffness matrix has the form

$$\mathbf{K}_m^H = \beta_m E4J_0 \sum_{f=1}^{2}\sum_{K=1}^{4} \frac{J_K}{A^f}\left(\mathbf{B}_m^{KH}\right)_{12}^{T}\left(\mathbf{B}_m^{KH}\right)_{12}. \tag{43}$$

For large strain elastic–plastic problems, the stabilization forces defined above may introduce a too large relative stiffness if the elastic module is used. To prevent this the plastification level may be considered to compute a knock-down factor for the elastic module. Then with the elastic strain across the thickness computed as

$$e_{12}^{e}(\zeta) = e_{12}(\zeta) - e_{12}^{p}(\zeta) \tag{44}$$

the following ratio is defined

$$R^f = \frac{2}{h}\int_h L^f(\zeta)\frac{e_{12}^{e}(\zeta)}{e_{12}(\zeta)}dh \tag{45}$$

to be used as knock-down factor on the elastic module in (41).

3.2. Transverse shear components

In order to approximate the most relevant components associated with transverse shear let us consider the square master element in local coordinates (ξ, η) corresponding to each external faces ($\zeta = \pm 1$) (see Fig. 1 left). In each of these faces the following interpolation will be used for the transverse shear components [16]:

$$\begin{bmatrix} C_{\xi 3} \\ C_{\eta 3} \end{bmatrix} = \frac{1}{2}\begin{bmatrix} 0 & 1-\eta & 0 & 1+\eta \\ 1-\xi & 0 & 1+\xi & 0 \end{bmatrix}\begin{bmatrix} C_{\eta 3}^{A} \\ C_{\xi 3}^{B} \\ C_{\eta 3}^{C} \\ C_{\xi 3}^{D} \end{bmatrix} = \mathbf{P}(\xi,\eta)\,\tilde{\mathbf{c}}$$

$$= \frac{1}{2}\begin{bmatrix} C_{\xi 3}^{B} + C_{\xi 3}^{D} \\ C_{\eta 3}^{A} + C_{\eta 3}^{C} \end{bmatrix} + \frac{1}{2}\begin{bmatrix} \eta\left(-C_{\xi 3}^{B} + C_{\xi 3}^{D}\right) \\ \xi\left(-C_{\eta 3}^{A} + C_{\eta 3}^{C}\right) \end{bmatrix} = \mathbf{P}_0\,\tilde{\mathbf{c}} + \mathbf{P}^H(\xi,\eta)\,\tilde{\mathbf{c}} \tag{46}$$

where these transverse shear components are defined in a mixed system, i.e. that includes natural coordinates in the plane and the spatial coordinate in the transverse direction (ξ, η, y_3). The components of interest are computed in terms of the gradient along the side and the gradient in normal direction $\mathbf{t}_3$ at the four points indicated as A ($\xi = -1, \eta = 0$), B ($\xi = 0, \eta = -1$), C ($\xi = 1, \eta = 0$) and D ($\xi = 0, \eta = 1$) (see Fig. 1 right). As can be seen in (46) each interpolated component is kept constant along a natural coordinate and varies linearly in the other natural coordinate. Note that the

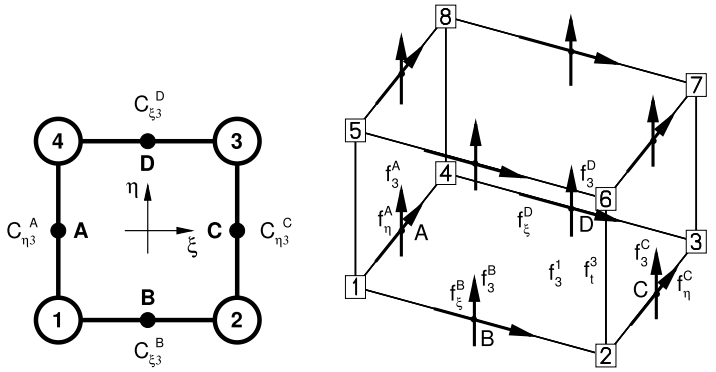

Fig. 1. Sampling points of the transverse shear components of the hexahedron.

points A–D are the same points ($K = 1, 4$) of the previous section where the local system has been defined and the in-plane components of tensor $\mathbf{C}$ have been computed.

The mixed components computed at the sampling points of each face are:

$$\tilde{\mathbf{c}} = \begin{bmatrix} C^A_{\eta 3} \\ C^B_{\xi 3} \\ C^C_{\eta 3} \\ C^D_{\xi 3} \end{bmatrix} = \begin{bmatrix} \mathbf{f}^A_\eta \cdot \mathbf{f}^A_3 \\ \mathbf{f}^B_\xi \cdot \mathbf{f}^B_3 \\ \mathbf{f}^C_\eta \cdot \mathbf{f}^C_3 \\ \mathbf{f}^D_\xi \cdot \mathbf{f}^D_3 \end{bmatrix} \tag{47}$$

that together with (46) allow to compute:

$$\tilde{\mathbf{C}}_2 = C_{\xi 3}\left(\mathbf{t}^\xi \otimes \mathbf{t}^3 + \mathbf{t}^3 \otimes \mathbf{t}^\xi\right) + C_{\eta 3}\left(\mathbf{t}^\eta \otimes \mathbf{t}^3 + \mathbf{t}^3 \otimes \mathbf{t}^\eta\right) \tag{48}$$

where $\begin{bmatrix}\mathbf{t}^\xi & \mathbf{t}^\eta & \mathbf{t}^3\end{bmatrix}$ are the dual base vectors of the local triad $\begin{bmatrix}\mathbf{t}_\xi & \mathbf{t}_\eta \mathbf{t}_3\end{bmatrix} = \begin{bmatrix}\frac{\partial \mathbf{X}}{\partial \xi} & \frac{\partial \mathbf{X}}{\partial \eta} & \frac{\partial \mathbf{X}}{\partial y_3}\end{bmatrix}$, so that a modified Cartesian component is

$$\bar{C}_{13} = \mathbf{t}_1 \cdot \bar{\mathbf{C}}_2 \cdot \mathbf{t}_3 = \mathbf{t}_1 \cdot \left[C_{\xi 3}\left(\mathbf{t}^\xi \otimes \mathbf{t}^3 + \mathbf{t}^3 \otimes \mathbf{t}^\xi\right) + C_{\eta 3}\left(\mathbf{t}^\eta \otimes \mathbf{t}^3 + \mathbf{t}^3 \otimes \mathbf{t}^\eta\right)\right] \cdot \mathbf{t}_3 \tag{49}$$

denoting by $a^j_i = \mathbf{t}_i \cdot \mathbf{t}^j$ (with $i = 1, 2, 3$ and $j = \xi, \eta, 3$)

$$\bar{C}_{13} = C_{\xi 3}\left(a^\xi_1 a^3_3 + a^3_1 a^\xi_3\right) + C_{\eta 3}\left(a^\eta_1 a^3_3 + a^3_1 a^\eta_\eta\right) = C_{\xi 3} a^\xi_1 + C_{\eta 3} a^\eta_1 \tag{50}$$

and similarly for the other component of interest ($\bar{C}_{23}$). Using the condition $a^3_i = \delta^3_i$ it reduces to

$$\begin{bmatrix}\bar{C}_{13} \\ \bar{C}_{23}\end{bmatrix} = \begin{bmatrix} a^\xi_1 & a^\eta_1 \\ a^\xi_2 & a^\eta_2 \end{bmatrix} \begin{bmatrix} C_{\xi 3} \\ C_{\eta 3} \end{bmatrix} = \mathbf{J}^{-1}_p \begin{bmatrix} C_{\xi 3} \\ C_{\eta 3} \end{bmatrix} \tag{51}$$

where $\mathbf{J}^{-1}_p$ is the inverse Jacobian matrix of the isoparametric interpolation restricted to the face tangent plane. Note that these components are null in the reference configuration.

The components of interest of the deformation gradient in the natural system at the sampling points A–D (47) are obtained using the derivatives of the shape functions (Eq. (3)) that depend only on the nodes of each face. In contrast the gradient in the transverse direction depends on the eight node of the element. The components of $\bar{\mathbf{C}}^s$ at each face in the local Cartesian system are then obtained by replacing (47) in (46), evaluate them at the face center and transform

to Cartesian coordinates (51)

$$\begin{bmatrix}\bar{C}_{13}\\ \bar{C}_{23}\end{bmatrix}^f = \mathbf{J}_p^{-1}\mathbf{P}_0\begin{bmatrix}\mathbf{f}_\eta^A\cdot\mathbf{f}_3^A\\ \mathbf{f}_\xi^B\cdot\mathbf{f}_3^B\\ \mathbf{f}_\eta^C\cdot\mathbf{f}_3^C\\ \mathbf{f}_\xi^D\cdot\mathbf{f}_3^D\end{bmatrix}^f = \mathbf{J}_p^{-1}\mathbf{P}_0\tilde{\mathbf{c}}^f \tag{52}$$

$$= \frac{1}{2}\mathbf{J}_p^{-1}\begin{bmatrix}C_{\xi 3}^B + C_{\xi 3}^D\\ C_{\eta 3}^A + C_{\eta 3}^C\end{bmatrix}^f \tag{53}$$

and finally interpolate to the integration points along the element axis:

$$\bar{\mathbf{C}}^s = L^1(\zeta)\,\bar{\mathbf{C}}^{s1} + L^2(\zeta)\,\bar{\mathbf{C}}^{s2}. \tag{54}$$

The matrix relating incremental displacements with incremental strains $\bar{\mathbf{B}}_s$, require first the evaluation at the sampling points

$$\tilde{\mathbf{B}}_s\delta\mathbf{u}^e = \begin{bmatrix}\mathbf{f}_\eta^A\cdot\boldsymbol{\delta}\mathbf{f}_3^A + \boldsymbol{\delta}\mathbf{f}_\eta^A\cdot\mathbf{f}_3^A\\ \mathbf{f}_\xi^B\cdot\delta\mathbf{f}_3^B + \boldsymbol{\delta}\mathbf{f}_\xi^B\cdot\mathbf{f}_3^B\\ \mathbf{f}_\eta^C\cdot\boldsymbol{\delta}\mathbf{f}_3^C + \delta\mathbf{f}_\eta^C\cdot\mathbf{f}_3^C\\ \mathbf{f}_\xi^D\cdot\boldsymbol{\delta}\mathbf{f}_3^D + \boldsymbol{\delta}\mathbf{f}_\xi^D\cdot\mathbf{f}_3^D\end{bmatrix} \tag{55}$$

where $\delta\mathbf{x}^e = \delta\mathbf{u}^e$ and transform to the Cartesian system at each face center

$$\bar{\mathbf{B}}_s^f = \mathbf{J}_p^{-1}\mathbf{P}_0\tilde{\mathbf{B}}_s^f \tag{56}$$

and finally interpolate to the integration points using

$$\bar{\mathbf{B}}_s = L^1(\zeta)\,\bar{\mathbf{B}}_s^1 + L^2(\zeta)\,\bar{\mathbf{B}}_s^2. \tag{57}$$

While the equivalent nodal forces may be expressed as:

$$\begin{aligned}\mathbf{r}_s^T &= \int_V \begin{bmatrix}S_{13}\\ S_{23}\end{bmatrix}^T \left[\bar{\mathbf{B}}_s\right]_{2\times 24} dV\\ &= \int_{-1}^{1}\mathbf{Q}^T\left[\bar{\mathbf{B}}_s^1 L^1 + \bar{\mathbf{B}}_s^2 L^2\right]_{2\times 24} J d\zeta\\ &= \int_{-1}^{1} A\mathbf{Q}^T L^1 J d\zeta\bar{\mathbf{B}}_s^1 + \int_{-1}^{1} A\mathbf{Q}^T L^2 J d\zeta\bar{\mathbf{B}}_s^2\\ &= \bar{\mathbf{Q}}_{4\times 1}^T\begin{bmatrix}\bar{\mathbf{B}}_s^1\\ \bar{\mathbf{B}}_s^2\end{bmatrix}_{4\times 24}\end{aligned} \tag{58}$$

where a sort of generalized shear forces $\bar{\mathbf{Q}}$ may be defined at each element as:

$$\bar{\mathbf{Q}}_{4\times 1} = \int_{-1}^{1}\begin{bmatrix}\begin{bmatrix}S_{13}\\ S_{23}\end{bmatrix}L^1\\ \begin{bmatrix}S_{13}\\ S_{23}\end{bmatrix}L^2\end{bmatrix} J d\zeta. \tag{59}$$

3.2.1. Geometric stiffness matrix computation based on $\bar{\mathbf{Q}}$

With the above definitions the geometric stiffness matrix is obtained from:

$$\delta\mathbf{u}^T\mathbf{K}_s^G\Delta\mathbf{u} = \Delta\left\{\begin{bmatrix}\bar{\mathbf{B}}_s^1\\ \bar{\mathbf{B}}_s^2\end{bmatrix}\delta\mathbf{u}\right\}^T\bar{\mathbf{Q}}. \tag{60}$$

For instance the contribution from the lower face results

$$\frac{1}{2}\left[\bar{Q}_1, \bar{Q}_2\right]\mathbf{J}_p^{-1}\begin{bmatrix}\mathbf{f}_\xi^B\cdot\delta\mathbf{f}_3^B+\delta\mathbf{f}_\xi^B\cdot\mathbf{f}_3^B+\mathbf{f}_\xi^D\cdot\delta\mathbf{f}_3^D+\delta\mathbf{f}_\xi^D\cdot\mathbf{f}_3^D\\ \mathbf{f}_\eta^A\cdot\delta\mathbf{f}_3^A+\delta\mathbf{f}_\eta^A\cdot\mathbf{f}_3^A+\mathbf{f}_\eta^C\cdot\delta\mathbf{f}_3^C+\delta\mathbf{f}_\eta^C\cdot\mathbf{f}_3^C\end{bmatrix}^1 \tag{61}$$

where calling

$$\left[\bar{Q}_1', \bar{Q}_2'\right] = \left[\bar{Q}_1, \bar{Q}_2\right]\mathbf{J}_p^{-1} \tag{62}$$

is

$$\frac{1}{2}\begin{pmatrix}\bar{Q}_1'\Delta\left(\mathbf{f}_\xi^B\cdot\delta\mathbf{f}_3^B+\delta\mathbf{f}_\xi^B\cdot\mathbf{f}_3^B+\mathbf{f}_\xi^D\cdot\delta\mathbf{f}_3^D+\delta\mathbf{f}_\xi^D\cdot\mathbf{f}_3^D\right)+\\ \bar{Q}_2'\Delta\left(\mathbf{f}_\eta^A\cdot\delta\mathbf{f}_3^A+\delta\mathbf{f}_\eta^A\cdot\mathbf{f}_3^A+\mathbf{f}_\eta^C\cdot\delta\mathbf{f}_3^C+\delta\mathbf{f}_\eta^C\cdot\mathbf{f}_3^C\right)\end{pmatrix}. \tag{63}$$

The derivatives $N_3^{J(K)}$ associated with $\mathbf{f}_3$ may be stored in an array for each face. Those associated with $\mathbf{f}_t$, involving 2 nodes at each derivative, are not stored as they have values 0, 1 or -1 so they may be included explicitly in the codification.

3.2.2. Shear stabilization

The components in (46) not used for the shear strain computations along the element axis may be used to stabilize the sub integrated scheme. They are

$$\begin{bmatrix}\varepsilon_{\xi 3}\\ \varepsilon_{\eta 3}\end{bmatrix} = \frac{1}{2}\begin{bmatrix}\eta\left(-C_{\xi 3}^B+C_{\xi 3}^D\right)\\ \xi\left(-C_{\eta 3}^A+C_{\eta 3}^C\right)\end{bmatrix} = \mathbf{P}^H(\xi,\eta)\,\tilde{\mathbf{c}}. \tag{64}$$

Using the same $\mathbf{J}_p^{-1}$ computed at each face center, associated shear forces may be defined using the transverse shear modulus G multiplied by a factor $\beta_s \ll 1$. The stabilization strain energy in this case can be approximated by

$$W_s^H = \frac{\beta_s G J_0}{2}\sum_{f=1}^{2}\int_\square\left\{\begin{bmatrix}\varepsilon_{\xi 3} & \varepsilon_{\eta 3}\end{bmatrix}\mathbf{J}_p^{-T}\mathbf{J}_p^{-1}\begin{bmatrix}\varepsilon_{\xi 3}\\ \varepsilon_{\eta 3}\end{bmatrix}\right\}^f d\xi\, d\eta \tag{65}$$

denoting the components of the symmetric matrix

$$\begin{bmatrix}a & c\\ c & b\end{bmatrix} = \mathbf{J}_p^{-T}\mathbf{J}_p^{-1} \tag{66}$$

a further approximation to the integral (reasonable accurate for stabilization purposes) is:

$$W^H = \frac{\beta_s G J_0}{2}\frac{4}{9}\sum_{f=1}^{2}\left\{b\left(-C_{\eta 3}^A+C_{\eta 3}^C\right)^2+a\left(-C_{\xi 3}^B+C_{\xi 3}^D\right)^2\right\}^f. \tag{67}$$

Denoting at each face by

$$\begin{bmatrix}\sigma_\xi\\ \sigma_\eta\end{bmatrix} = \frac{4}{9}\beta_s G J_0\begin{bmatrix}a\left(-C_{\xi 3}^B+C_{\xi 3}^D\right)\\ b\left(-C_{\eta 3}^A+C_{\eta 3}^C\right)\end{bmatrix} \tag{68}$$

the associated nodal forces result

$$\mathbf{r}_s^{HT} = \sum_{f=1}^{2} \begin{bmatrix} \sigma_\xi & \sigma_\eta \end{bmatrix} \begin{bmatrix} -\tilde{\mathbf{B}}_{sB} + \tilde{\mathbf{B}}_{sD} \\ -\tilde{\mathbf{B}}_{sA} + \tilde{\mathbf{B}}_{sC} \end{bmatrix}_{2\times 24}. \tag{69}$$

Finally the stiffness matrix related to the transverse shear stabilization is

$$\mathbf{K}_s^H = \frac{4}{9}\beta_s G J_0 \sum_{f=1}^{2} \begin{bmatrix} -\tilde{\mathbf{B}}_{sB} + \tilde{\mathbf{B}}_{sD} \\ -\tilde{\mathbf{B}}_{sA} + \tilde{\mathbf{B}}_{sC} \end{bmatrix}_{2\times 24}^{T} \begin{bmatrix} a & \\ & b \end{bmatrix} \begin{bmatrix} -\tilde{\mathbf{B}}_{sB} + \tilde{\mathbf{B}}_{sD} \\ -\tilde{\mathbf{B}}_{sA} + \tilde{\mathbf{B}}_{sC} \end{bmatrix}_{2\times 24}. \tag{70}$$

3.3. Transverse normal component

To avoid the locking due to the Poisson effect in bending dominated problems, an enhanced assumed technique is used for the component $\mathbf{C}^t$. Only the Cartesian component C_{33} is of interest so here the EAS technique departs slightly from the standard form and follows the proposal in [23] as explained next.

3.3.1. Enhanced assumed strain

At the element center ($\xi = \eta = \zeta = 0$) the Cartesian derivative in direction y_3 of the deformation gradient is computed using the isoparametric interpolation

$$\mathbf{f}_3^C = \sum_{I=1}^{8} N_3^{IC} \mathbf{x}^I. \tag{71}$$

The enhanced version of this gradient is defined as

$$\bar{\mathbf{f}}_3 = \mathbf{f}_3^C e^{\alpha\zeta} \tag{72}$$

so that the enhanced component of interest C_{33} is

$$\bar{C}_{33} = \mathbf{f}_3^C \cdot \mathbf{f}_3^C e^{2\alpha\zeta} = C_{33}^C e^{2\alpha\zeta}. \tag{73}$$

In a first approximation the transverse normal strain is (remind the way the geometry is assumed to be meshed)

$$\bar{e}_{33} \simeq \frac{1}{2} \ln\left(C_{33}^C e^{2\alpha\zeta}\right) = e_{33}^C + \alpha\zeta. \tag{74}$$

In this approach the changes this enhanced $\bar{\mathbf{f}}_3$ may produce in other components of the right Cauchy–Green tensor are disregarded, as those components have already been computed in the previous section.

3.3.2. Balance equation and implicit solution

The variation of the Green strain includes now the internal DOF α

$$\begin{aligned} \delta\bar{E}_{33} &= \delta\mathbf{f}_3^C \cdot \mathbf{f}_3^C e^{2\alpha\zeta} + \bar{C}_{33}\zeta\,\delta\alpha \\ &= e^{2\alpha\zeta}\mathbf{B}_3^C \delta\mathbf{u}^e + \bar{C}_{33}\zeta\,\delta\alpha \end{aligned} \tag{75}$$

where the first term replaces the corresponding part in the approach formulated exclusively in displacements (the only difference is the factor $e^{2\alpha\zeta}$ in the component associated to δE_{33}).

The balance equation (15) associated to the variable α is

$$\delta\alpha \int_{-1}^{1} S_{33}\bar{C}_{33}\zeta\, J d\zeta = \delta\alpha\, r_\alpha = 0 \tag{76}$$

and a Newton–Raphson technique allows to determine the value of α that cancels the residue r_α

$$\int_{-1}^{1} \left[\frac{\partial S_{33}\bar{C}_{33}}{\partial \mathbf{u}} \Delta\mathbf{u} + \frac{\partial S_{33}\bar{C}_{33}}{\partial \alpha}\Delta\alpha\right] \zeta\, J d\zeta + r_\alpha = 0 \tag{77}$$

with

$$\frac{\partial S_{33}\bar{C}_{33}}{\partial \mathbf{u}} = \bar{C}_{33}\mathbf{D}_3\bar{\mathbf{B}} + 2S_{33}e^{2\alpha\zeta}\mathbf{B}_3^C = \bar{C}_{33}\mathbf{D}_3\bar{\mathbf{B}} + 2S_{33}\bar{\mathbf{B}}_3 \tag{78}$$

$$\frac{\partial S_{33}\bar{C}_{33}}{\partial \alpha} = \bar{C}_{33}D_{33}\bar{C}_{33}\zeta + 2S_{33}\bar{C}_{33}\zeta = \bar{C}_{33}\left(D_{33}\bar{C}_{33}\zeta + 2S_{33}\zeta\right) \tag{79}$$

where $\mathbf{D}$ is the tangent constitutive matrix (Voigt's notation), the subscript 3 indicates the third row (or column) so that D_{33} is the diagonal component. By $\bar{\mathbf{B}}$ it is denoted the matrix relating increments in Green–Lagrange strains and displacements changes for the assumed strain approaches used for tensor $\mathbf{C}$ components as described above.

For implicit solutions techniques, the internal DOF α is locally condensed at each element using Eq. (77):

$$\begin{aligned}\int_{-1}^{1}\left[\left(\bar{C}_{33}\mathbf{D}_3\bar{\mathbf{B}} + 2S_{33}\bar{\mathbf{B}}_3\right)\Delta\mathbf{u} + \bar{C}_{33}\left(D_{33}\bar{C}_{33}\zeta + 2S_{33}\zeta\right)\Delta\alpha\right]\zeta J d\zeta = 0\\ \mathbf{H}\Delta\mathbf{u} + k_\alpha\Delta\alpha + r_\alpha = 0\end{aligned} \tag{80}$$

then

$$\Delta\alpha = -\frac{r_\alpha}{k_\alpha} - \frac{1}{k_\alpha}\mathbf{H}\Delta\mathbf{u} \tag{81}$$

that can be replaced in the balance equation associated to the displacement variations (14)

$$\delta\mathbf{u}^T\int_V \bar{\mathbf{B}}^T\mathbf{S}dV - \delta\mathbf{u}^T G_{ext} = \delta\mathbf{u}^T\mathbf{r}\left(\mathbf{u},\alpha\right) \tag{82}$$

once linearized that leads to

$$\begin{aligned}\int_{-1}^{1}\left[\bar{\mathbf{B}}^T\left(\frac{\partial\mathbf{S}}{\partial\mathbf{u}}\Delta\mathbf{u} + \frac{\partial\mathbf{S}}{\partial\alpha}\Delta\alpha\right) + \mathbf{S}\left(\frac{\partial\bar{\mathbf{B}}}{\partial\mathbf{u}}\Delta\mathbf{u} + \frac{\partial\bar{\mathbf{B}}}{\partial\alpha}\Delta\alpha\right)\right]Jd\zeta + \mathbf{r}\left(\mathbf{u}\right) &= \mathbf{0}\\ \left(\mathbf{K}_T\Delta\mathbf{u} + \mathbf{H}^T\Delta\alpha\right) + \mathbf{r}\left(\mathbf{u}\right) &= \mathbf{0}\\ \left(\mathbf{K}_T - \mathbf{H}^T\frac{1}{k_\alpha}\mathbf{H}\right)\Delta\mathbf{u} - \mathbf{H}^T\frac{r_\alpha}{k_\alpha} + \mathbf{r}\left(\mathbf{u}\right) &= \mathbf{0}.\end{aligned} \tag{83}$$

The contributions of this last expression to the Newton–Raphson scheme are:

$$\bar{\mathbf{K}}_T = \mathbf{K}_T - \mathbf{H}^T\frac{1}{k_\alpha}\mathbf{H} \tag{84}$$

$$\bar{\mathbf{r}} = \mathbf{r} - \mathbf{H}^T\frac{r_\alpha}{k_\alpha}. \tag{85}$$

Note that above

$$k_\alpha = \int_{-1}^{1}\bar{C}_{33}\left(D_{33}\bar{C}_{33} + 2S_{33}\right)\zeta^2 Jd\zeta \tag{86}$$

$$\mathbf{H} = \int_{-1}^{1}\left(\bar{C}_{33}\mathbf{D}_3\bar{\mathbf{B}} + 2S_{33}\bar{\mathbf{B}}_3\right)\zeta Jd\zeta \tag{87}$$

where $\mathbf{K}_T$ is the tangent stiffness matrix computed as the sum of the material part

$$\mathbf{K}_M = \int_{-1}^{1}\bar{\mathbf{B}}^T\mathbf{D}\bar{\mathbf{B}}Jd\zeta \tag{88}$$

and the geometric part, whose contributions due to the membrane and shear parts have been obtained above.

3.3.3. Geometric stiffness matrix

The contribution to the equivalent nodal forces of the transverse normal component may be written as

$$\mathbf{r}_t = \int_V \mathbf{B}_3 S_{33} dV = \int_{-1}^{1} e^{2\alpha\zeta} \mathbf{B}_3^C S_{33} J d\zeta = \mathbf{B}_3^C \bar{S}_{33} \tag{89}$$

where

$$\bar{S}_{33} = \int_{-1}^{1} e^{2\alpha\zeta} S_{33} J d\zeta \tag{90}$$

then the contribution to the geometric stiffness is:

$$\delta\mathbf{u}^T \mathbf{K}_{Gt} \Delta\mathbf{u} = \sum_{I=1}^{8} \left(\delta\mathbf{u}^I\right)^T \sum_{J=1}^{8} N_3^{IC} N_3^{JC} \bar{S}_{33} \begin{bmatrix} 1 & & \\ & 1 & \\ & & 1 \end{bmatrix} \Delta\mathbf{u}^J. \tag{91}$$

3.3.4. Explicit solution

In the above implicit integration scheme the element database may include, to avoid its recomputation: k_α and vector $\mathbf{H}$ (besides α that is essential) that implies an important increase in the storage space. Also it requires the computation of $\mathbf{D}_3$ (relating elastic–plastic increments of the Piola–Kirchhoff stress tensor and Green–Lagrange strains).

For implicit solutions and approximations with a large number (12) of additional DOFs Simo et al. [19] suggest not to keep the submatrices (here reduced to vector $\mathbf{H}$ and scalar k_α) and to update iteratively the internal DOFs at the routine that computes stresses and equivalent nodal forces. They claim that a couple of iterations provide accurate enough results. In explicit codes an iteration in the computation of stresses is proportionally very costly, furthermore the elastic–plastic constitutive matrix $\mathbf{D}$ is not computed. Numerical experiments indicate that a single iteration using the elastic component D_{33} gives accurate results due to the small changes occurring in explicit integration [23].

The scheme proposed includes three stages where $\mathbf{D}$ is not computed and k_α and $\mathbf{H}$ are not stored:

1. Use $\bar{\mathbf{r}}$ from (85) as equivalent nodal forces and compute a first update of the EAS variable

$$\hat{\alpha}_{n+1} = \alpha_n - \frac{r_\alpha}{k_\alpha}. \tag{92}$$

2. Using the standard central difference scheme compute the incremental displacements $\Delta\mathbf{u}$.
3. Perform a second update of the EAS variable

$$\alpha_{n+1} = \hat{\alpha}_{n+1} - \frac{\mathbf{H}\Delta\mathbf{u}}{k_\alpha}. \tag{93}$$

4. Examples

In the set of numerical examples presented below, the element developed above is denoted by `SS`. Also with comparative purposes results obtained with other elements are included. `BBST` denotes a rotation-free triangular classical shell element [28], while `Solag` is an 8-node solid element with an averaged volumetric strain (4 integration points for the deviatoric part) and an assumed strain approach for the transverse shear [27] that allows to simulate shell under moderate/large strains using more than one layer of elements across the thickness. The elastic–plastic constitutive models implemented in these two elements are identical to the ones used in present element. This precludes differences in behavior associated to the constitutive or contact models in the numerical experiments. Also comparisons are made against `Q1SPs`, a reduced integration solid-shell element with an excellent performance [13, 12], and for the large displacements elastic case against the converged results published by Sze [29] obtained with the shell element `S4R` of a commercial code [30].

Regarding the stabilization factors β_m (see Eq. (39)) and β_s (see Eq. (65)) the usual practice is to use the lowest values possible as long as no stability problems are found in the simulations. For small strains such values may be in

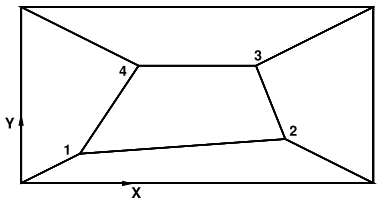

Coordinates [mm]
1: (0.04, 0.02)
2: (0.18, 0.03)
3: (0.16, 0.08)
4: (0.08, 0.08)

Fig. 2. Patch test geometry.

general lower than for large strains. Besides, for coarse meshes small values of the stabilization factors lead to larger displacements than elements with full integration and an apparently better behavior. This effect naturally disappears when the mesh is refined, and although it may be interesting to obtain displacements closer to converged values using coarse meshes, the use of low stabilization coefficients is not the proper way. In all the numerical simulations presented (small and large strains, coarse and fine meshes) the stabilization factors used were $\beta_m = \beta_s = 0.15$ than are reasonably conservative values. The same value has been used for both factors, although the most important is β_m as the results are quite less sensitive to β_s. In Sections 4.2, 4.4 and 4.7 some parametric studies of the influence of the stabilization factors are included to backup this choice.

4.1. Patch test

Fig. 2 shows a patch of elements that has been extensively used to assess quadrilateral shell elements and hexahedral solid-shell elements. The dimensions are: length $a = 0.24$ mm, width $b = 0.12$ mm, and thickness $t = 0.001$ mm. The lower surface has coordinate $z = -t/2$. The mechanical properties of the constitutive material are: elastic modulus $E = 10^6$ MPa and Poisson's ratio $\nu = 0.25$. As the problem is linear, only 2 integration points are used across the thickness located at the usual positions of the Gauss quadrature ($\zeta = \pm 1/\sqrt{3}$). Displacements are imposed at the nodes on the contour and computed at the inner nodes to assess the test.

For solid elements it is assumed that a necessary condition for convergence is that when the imposed displacements correspond with a constant gradient, constant stresses are obtained in all the elements. That case is denoted as the membrane patch test in this context. For shell elements a linear gradient is imposed across the thickness leading to a null transverse shear and a constant curvature tensor in all the elements (bending patch test). For solid-shell elements only the first test must be strictly passed, but if the target is to have a robust and reliable element the bending patch test must also be fulfilled.

4.1.1. Membrane patch test

The displacements (imposed in peripheral nodes) are associated to the linear field:

$$u_x = \left(x + \frac{y}{2}\right) \times 10^{-3} \qquad u_y = \left(y + \frac{x}{2}\right) \times 10^{-3} \tag{94}$$

and $u_z = 0$ only at the nodes in the lower face to allow the contraction due to Poisson effect. Using present element SS the correct results are obtained for both the displacements of the inner nodes as defined in (94) and the stresses at all integration points ($\sigma_{xx} = \sigma_{yy} = 1333.3$ MPa and $\sigma_{xy} = 400$ MPa). In all elements the internal DOF α is zero.

4.1.2. Bending patch test

The displacement field in this case is:

$$u_x = \left(x + \frac{y}{2}\right)\frac{z}{2} \times 10^{-3} \qquad u_y = \left(y + \frac{x}{2}\right)\frac{z}{2} \times 10^{-3} \qquad u_z = \left(x^2 + xy + y^2\right)\frac{1}{2} \times 10^{-3} \tag{95}$$

that is imposed on the boundary nodes of both shell faces. Again the computed results coincide with the expected values, for both the displacements given by expression (95) and the stresses at the Gauss points ($\sigma_{xx} = \sigma_{yy} = \pm 0.3849$ MPa and $\sigma_{xy} = \pm 0.1155$ MPa). The internal DOF in this case results $\alpha = 0.3333 \times 10^{-8}$ for all elements.

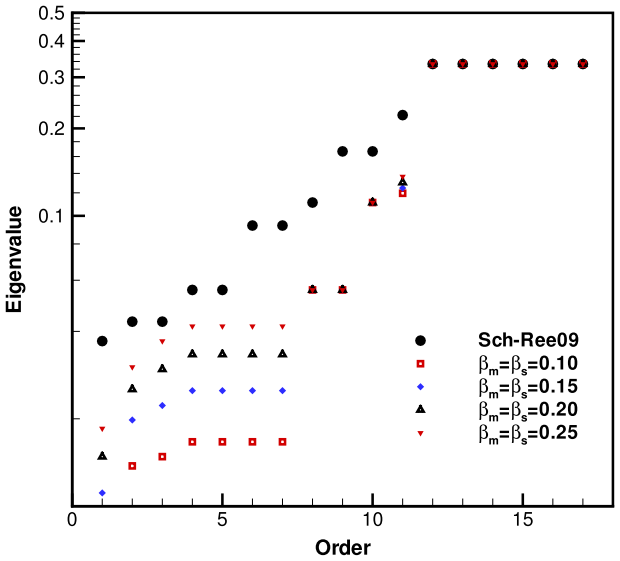

Fig. 3. Influence of β in eigenvalues.

4.2. Eigenvalue analysis

In order to assess the influence of the stabilization factors, the eigenvalues of the stiffness matrix of an undeformed element of side length 1.0 mm in the nearly incompressible limit ($E = 1.0$ N/mm^2 and $\nu = 0.499999$) are computed considering different values of $\beta_s = \beta_m$. Six null eigenvalues are found for all β values considered, then the test shows that the proposed hourglass stabilization does not exhibit any rank deficiency of the element stiffness matrix. In Fig. 3 the non-zero eigenvalues are plotted together with the results of [31]. The 12th until 17th ones agree with the results of the quoted reference and others [32,33,11] while for the largest eigenvalue (not shown in the figure) associated to the "breathing mode" a constant value of 250×10^3 is computed for all β. Therefore, it can be stated that the element is free of volumetric locking.

4.3. Cantilever beam under point load

A clamped-free beam of length $L = 10$ mm, width $B = 1$ mm and thickness $t = 0.1$ mm is subjected to a normal point load $F = 40$ N at the free end. A Young's modulus of $E = 10^6$ MPa leads to a problem with large displacements but small elastic strains. The use of different Poisson's ratio ($\nu = 0.0$, $\nu = 0.3$ and $\nu = 0.4999$) allows to assess if the proposed approaches effectively eliminate the transverse shear, Poisson effect and volumetric lockings respectively.

Fig. 4(a) shows the original geometry and the deformed configuration obtained with ten equal load steps. The discretization includes 16 equally distributed elements along the length, one element in width, one across the thickness and two integration points. Fig. 4(b) plots the tip displacement as a function of the load factor λ[0:1] for the three different values of the Poisson ratio. The lowest value $\nu = 0$ allows to compare with the reference value ($u_z = 7.08$ mm) and assess if the approach for transverse shear effectively cures locking. The displacement obtained is $u_z = 7.05$ mm that indicates that the element is free of shear locking. The second value of Poisson's ratio ($\nu = 0.30$) allows to determine if the implemented EAS scheme avoids the locking due to Poisson effect. For this case the computed displacement is $u_z = 7.03$ mm, that although it is not exactly the same value, shows that this type of locking is avoided allowing to fit a linear variation of transverse normal strain. The largest value of Poisson's ratio (0.4999) lets us observe if there is a significant deterioration in the element performance in the quasi-incompressible range. In this last case the displacement obtained was $u_z = 7.00$ then it can be said that the influence of the different Poisson's ratio is small and that the different approaches have been successful to cure the different lockings. Finally the distorted mesh shown in Fig. 4(a) has been used to assess the behavior of the present element with such an in-plane mesh distortion. The displacement obtained in this last case is denoted by "Dist-0.4999" in Fig. 4(b) where the final value is $u_z = 6.58$ that is 6% less than the value obtained with the uniform mesh.

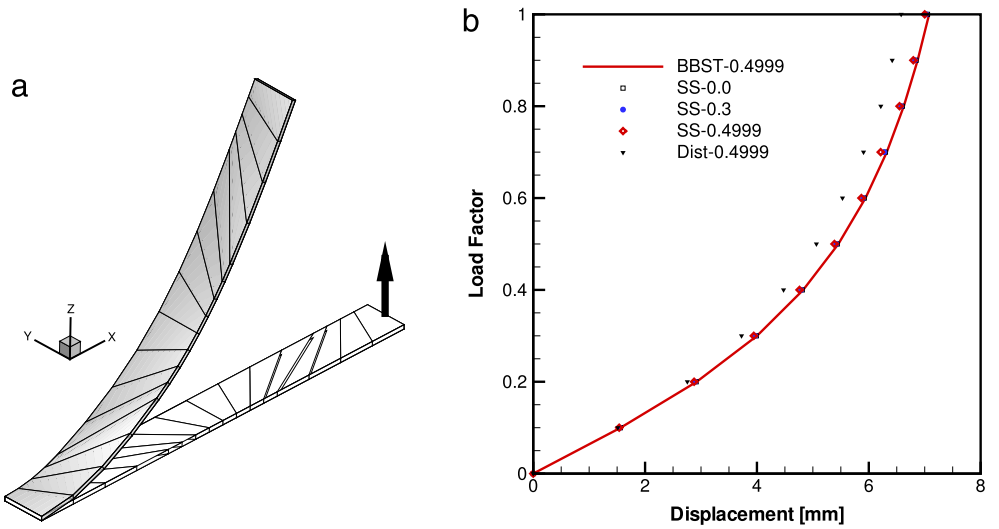

Fig. 4. Cantilever beam under point load.

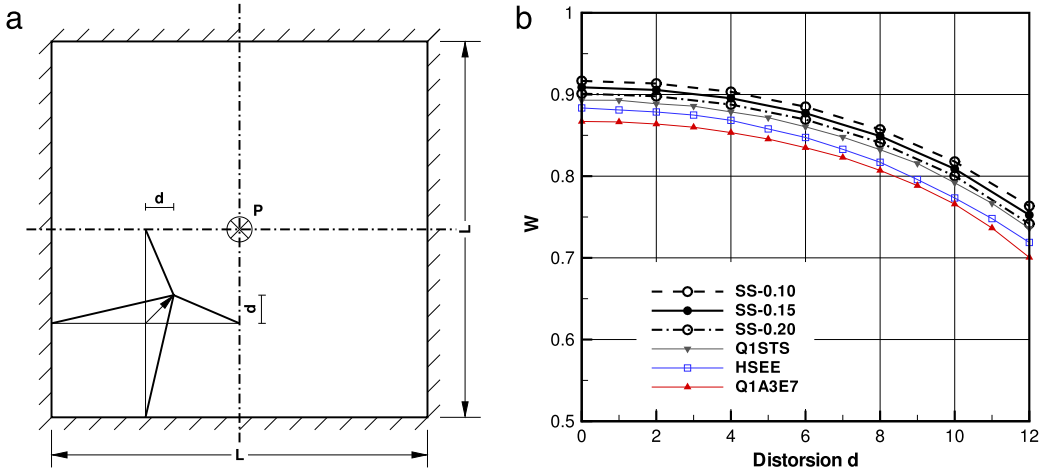

Fig. 5. Clamped square plate. Mesh distortion sensitivity.

4.4. *Square clamped plate under a point load*

The square plate fully clamped along all sides shown in Fig. 5(a) is widely used to assess in-plane distortion sensitivity. The side length is $L = 100$ mm with a thickness $t = 1$ mm. The mechanical properties of the material ($E = 10^4$ MPa and $\nu = 0.3$) and the central point load value ($P = 16.3527$ N) are chosen so that the analytic displacement at the center is $u_3^c = 1$ mm. Only four elements are used for the discretization taking advantage of the double symmetry. To assess distortion sensitivity the central node of the mesh is moved a distance $0 \leq d \leq 12$ mm as shown in Fig. 5(a). Fig. 5(b) plots the normalized displacement w as a function of the distortion parameter d for the present element (SS-β) and others published in the literature HSEE [34], Q1A3E7 [35] and Q1STs. To assess the influence of the stabilization factor, three different values of $\beta_s = \beta_m$ are considered. Clearly an increase of the of β leads to a stiffer behavior but the influence of the distortion parameter does not change. It can be seen that the distortion sensitivity is similar for all the elements compared and that the present element provides values closer to the analytic solution.

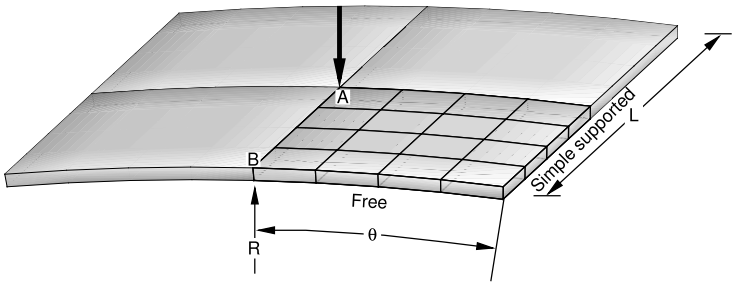

Fig. 6. Cylindrical panel with a point load.

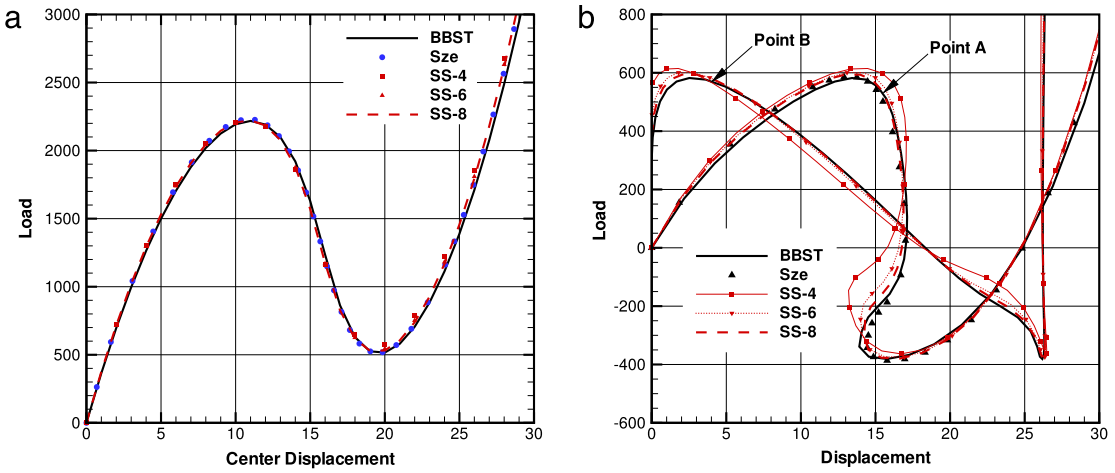

Fig. 7. Hinged cylindrical panel. (a) $t = 12.7$; (b) $t = 6.35$.

4.5. *Hinged cylindrical panel under point load*

This example considers a rectangular cylindrical panel simply supported along the straight sides, free along the curved sides and subjected to a normal point load in its center (see Fig. 6). The geometry of the middle surface is defined by the panel length $L = 508$ mm, the cylinder radius $R = 2540$ mm and half the subtended angle $\vartheta = 0.1$ rad. The equilibrium path of the system presents a limit point, followed by a strong resistance loss and a subsequent stiffening when the curvature is reversed. For the same middle surface geometry two different thicknesses values are considered $t = 12.7$ and $t = 6.35$ that leads for the thin case to a backward movement of the applied load. This example has been widely used in the literature to study the convergence properties of shell finite elements and path-following strategies.

Three discretizations with 4, 6 and 8 elements per side have been considered. One element is used in the thickness. If two elements across the thickness were used, the hinged condition can be easily imposed fixing the nodes in the middle surface for the straight sides. However results obtained with such a model are not strictly comparable with those obtained with shell elements. On the other hand, using just one element across the thickness requires to establish master–slave conditions between the corresponding nodes in the upper and lower surfaces ($\mathbf{u}^U = -\mathbf{u}^L$). The vertical displacement under the load point "A" (both thicknesses) and the vertical displacement of the center of the free edge "B" (for the thin case only) are used to assess the element behavior. Converged results obtained with the classical shell element `BBST` and those provided by Sze [29] are used for comparison. For the thick case (Fig. 7(a)) the displacement obtained with the mesh $6 \times 6 \times 1$ is practically coincident with the converged values of shell elements (`BBST` and `S4R`). For the thin case (Fig. 7(b)) the displacements obtained with the different meshes seem to converge to those obtained with shell elements. In this case the coarsest mesh is clearly not enough accurate for all the range of interest, particularly for the post-critical path where the loaded point moves backward.

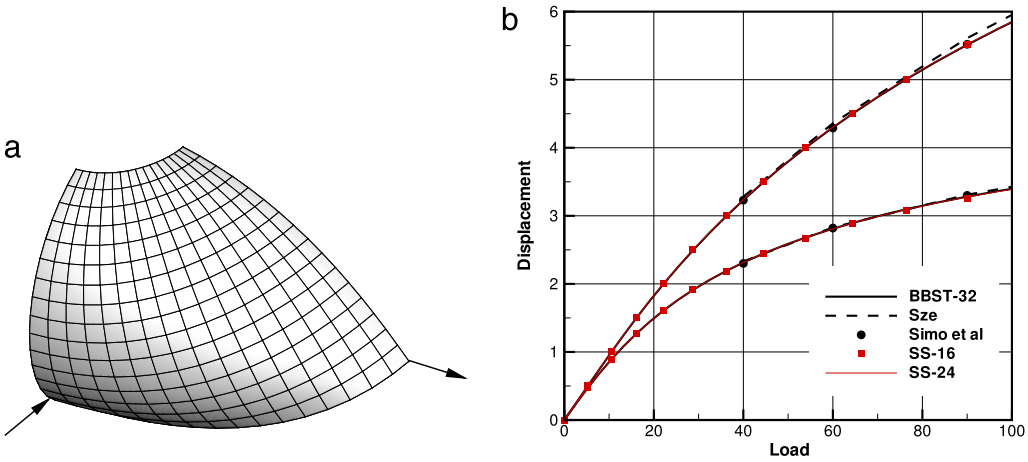

Fig. 8. Incomplete hemisphere under point loads. (a) Deformed geometry; (b) displacements of the loaded points.

Table 1
Convergence of the norm of the residual force during equilibrium iterations.

Iteration	Present	HSEE [34]
0	$6.25 \times 10^{+0}$	$6.25 \times 10^{+0}$
1	$4.32 \times 10^{+6}$	$3.51 \times 10^{+8}$
2	$6.87 \times 10^{+4}$	$4.57 \times 10^{+6}$
3	$4.22 \times 10^{+3}$	$9.05 \times 10^{+2}$
4	$1.50 \times 10^{+2}$	2.81×10^{-3}
5	$5.84 \times 10^{+1}$	
6	1.12×10^{-1}	

4.6. Incomplete hemisphere under point loads

This is a well known problem of a doubly curved shell in the context of large elastic deformations. Fig. 8 shows the quarter of the global deformed geometry considered due to symmetry. The response is basically inextensional where the membrane behavior is not relevant, and due to the double curvature the membrane and the Poisson effect lockings may be important. Two regular meshes with 16 and 24 elements per sides have been analyzed. The coarser mesh is usually used to determine if the element suffers of membrane locking due to the initial curvature, i.e. if the results differ by more than 5% from the correct ones it is because the element presents membrane locking. The middle surface radius is $R = 10$ mm and the thickness is $t = 0.04$ mm ($R/t = 250$). The mechanical properties are $E = 6.825 \times 10^4$ GPa and $\nu = 0.3$.

Fig. 8(a) shows the deformed configuration for an inward displacement of 60% of R. While Fig. 8(b) plots the displacement of the loaded point as a function of the load. The graph includes converged results obtained with element `BBST` using a mesh with 32 elements per side and the target results obtained independently by [29] and [36] with transverse shear deformable quadrilateral shell elements. The larger displacement corresponds to the point with the inward load and its sign has been reversed. For the present element the displacements with both meshes considered have been included. The results obtained with the 16 elements per side mesh are almost indistinguishable of those obtained with the 24 elements per side mesh. They are in excellent agreement with those reported by [36] and the converged results obtained with the classical shell element `BBST`.

Finally the convergence rate of the equilibrium iteration is examined. In Table 1 the equilibrium iterations for a first step are listed for the coarse mesh. The table includes values reported in [34] for a fully integrated hexahedron based on a mixed formulation that has excellent convergence properties. Clearly present element has a lower convergence rate than element HSEE but yet reasonable good.

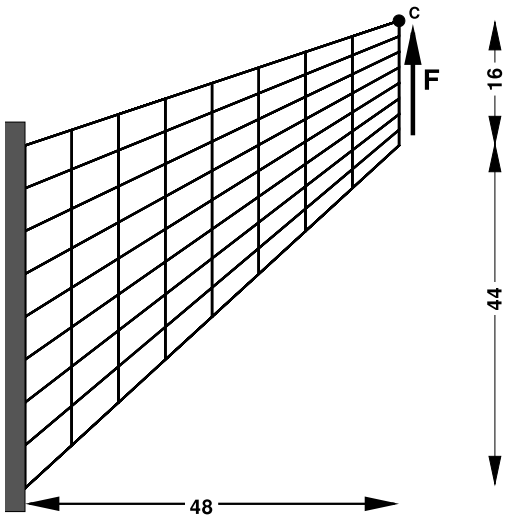

Fig. 9. Cook's membrane problem geometry, units in mm.

4.7. Cook's membrane problem

This example has been largely used as a benchmark for in-plane bending problems (see Fig. 9) for the assessment of two dimensional solid finite elements but other authors have also considered it for the assessment of 3D solid elements [34,15,9] and in commercial finite element codes [30]. Initially proposed as a elastic plane stress problem with linear kinematics, the same geometry was later used for both geometric and material nonlinearities in plane strain condition as will be considered here. This example allows to assess the in-plane approach for moderate strains independently of the other two approaches (ANS transverse shear and EAS transverse strain). Two material models are used: (a) a quasi-incompressible elastic material with shear modulus $G = 80.1938$ GPa and bulk modulus $K = 40.1 \times 10^4$ GPa associated with a Poisson ratio $\nu = 0.4999$ and (b) an elastic–plastic material with elastic properties $G = 80.1938$ GPa and $K = 164.21$ GPa (Poisson ratio $\nu = 0.29$) and J_2 plasticity with isotropic hardening defined by the function (e^p is the effective plastic strain and σ_y the yield stress):

$$\sigma_y = 0.45 + 0.12924e^p + (0.715 - 0.45)(1 - e^{-16.93e^p}) \text{ [GPa]}.$$

The applied load is 100 kN for the elastic material and 5 kN for the elastic–plastic material leading to a maximum equivalent plastic strain $e^p_{max} = 0.11$ than can be considered as a moderate strain problem.

Due to the problem setting (plane strain condition) the component $C_{33} = 1$ at all points ($\alpha = 0$), then the EAS scheme has no influence in this example (nor the transverse shear approach of course). The volumetric locking is avoided due to the reduced integration and the behavior of the in-plane formulation can be assessed. Three different values of the stabilization factor β_m are considered to show its influence for this problem with a large amount of shear energy and to assess the element ability to distort. Fig. 10 shows the vertical displacement at C as the mesh is refined. Uniform structured meshes are used identified by the number of elements per side. For comparison purposes the results obtained with three 2D elements have been included. Two four-node quadrilaterals: `Q1P0` formulated entirely in displacements with a 2×2 integration rule for the shear components and an element average of the volumetric strain, and `Q1EA` [37] based on the EAS technique including four internal DOFs. And a linear triangle with a modified deformation gradient $\bar{\mathbf{F}}$ approach [38] that averages the volumetric strain over two adjacent elements (only results for the elastic case are presented). In Fig. 10(a), corresponding to the quasi-incompressible elastic model, it can be seen that due to reduced integration the proposed hexahedron shows a more flexible behavior than the quadrilaterals used for comparison, showing a faster convergence in the control displacement. This figure shows that the influence of β_m is limited to the coarse meshes and that a value of 0.15 is a judicious choice. On the other hand, for the elastic–plastic model (Fig. 10(b)) where the plastic flow is isochoric but the elastic part is compressible, the present element shows a similar behavior to the element `Q1P0`.

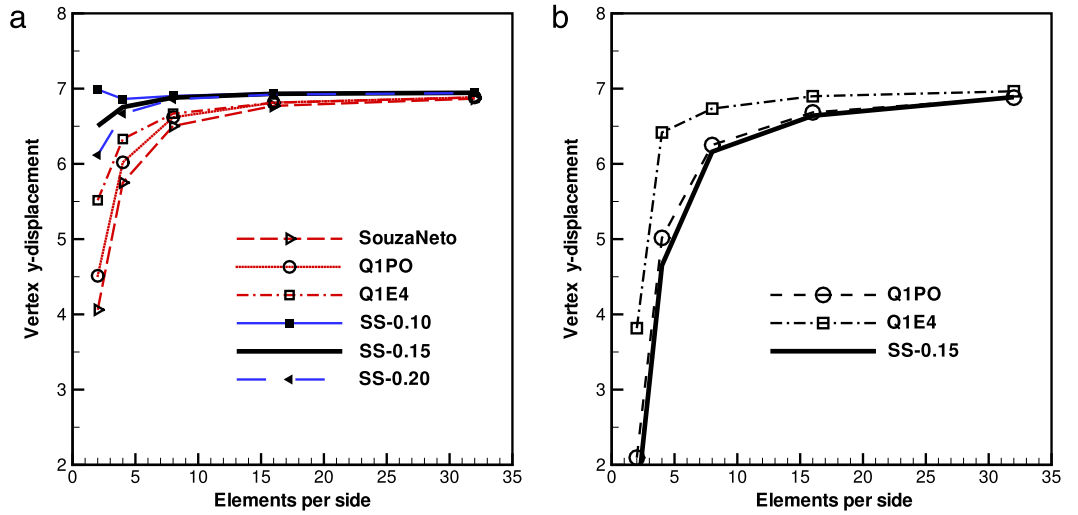

Fig. 10. Cook's membrane problem. (a) Elastic quasi-incompressible; (b) J_2 plasticity.

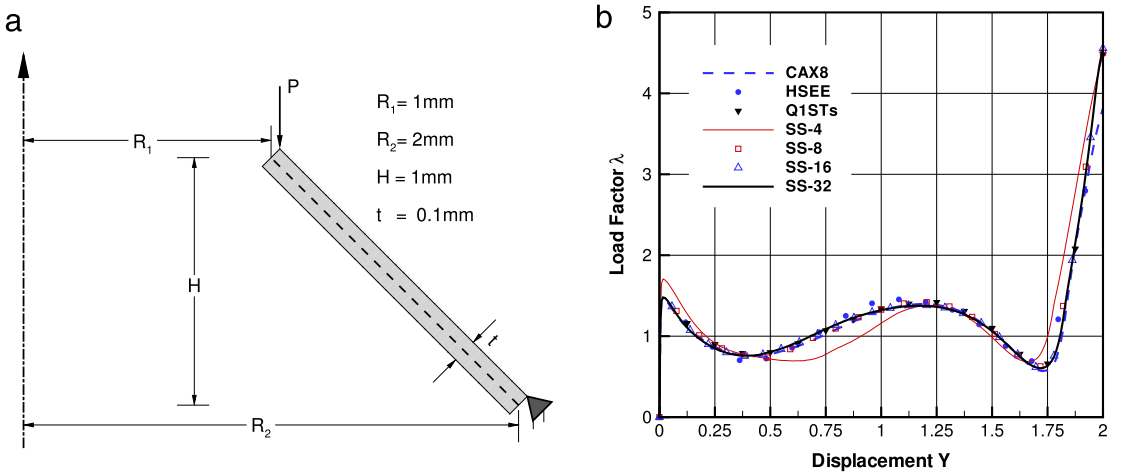

Fig. 11. Conical shell. (a) Geometry; (b) convergence study.

4.8. Conical shell

This is a second example with both geometric and material non-linearities that allows to assess the element under large elastic–plastic strains ($e^p_{max} \simeq 0.5$). The geometry has axial symmetry, the details are given in Fig. 11(a). The elastic properties are $E = 206.9$ MPa and $\nu = 0.29$ while the plastic model is J_2 plasticity (von Mises) with isotropic hardening ruled by the function

$$\sigma_y\left(e^p\right) = 0.45 + 0.12924e^p + 0.265\left(1 - e^{-16.93e^p}\right) \text{ [MPa]}.$$

The reference load is $P = 0.01$ N/mm that is scaled by the load factor λ.

Due to the axisymmetric geometry the discretization includes only one sector of $\theta = 0.1$ rad imposing adequate kinematic constrains. For the discretization of the meridian 4 meshes have been considered with 4, 8, 16 and 32 uniform divisions. In θ direction and thickness direction just one element is included with 5 integration points in the latter case. Fig. 11(b) plots the load factor as a function of the vertical displacement of the loaded line. The plot includes the results obtained with present element for the four meshes and converged results provided by [13] and [34] (HSEE) both discretizing one quarter of the total geometry. It can be seen that the results obtained using 8 elements along the meridian are practically converged ones. Also Fig. 11(b) includes results obtained with code Abaqus/std [30]

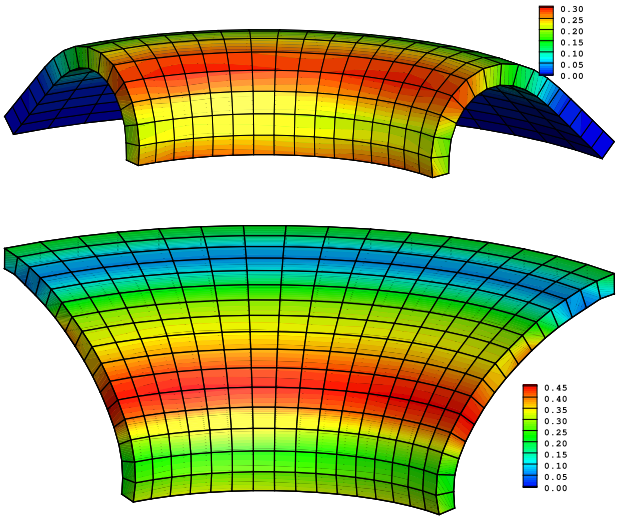

Fig. 12. Conical shell, deformed configuration and equivalent plastic strain for $u_y = 1$ and $u_y = 2$.

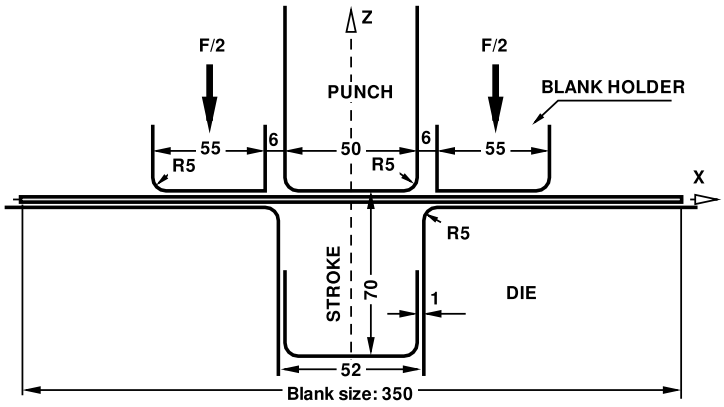

Fig. 13. 2D-deep drawing/springback of a strip.

using one row of elements CAX8 (quadratic Continuum AXilsymmetric 8-node element with full integration) that are in close agreement with present results but in the last part of the simulation where the line boundary conditions distort the end elements. Note that this example corresponds to a thick shell where membrane contribution to equilibrium is very important. Present results are in better agreement with the results published in [13] than those in [34]. Finally Fig. 12 shows the deformed configuration for half and the total loaded edge displacement, with a contour fill of the equivalent plastic strain. In this case one quarter of the total geometry has been discretized with a $16 \times 16 \times 1$ mesh.

4.9. Deep drawing and elastic springback

This example is one of the benchmarks proposed for Numisheet'93 [39]. Fig. 13 shows the tool's geometry, where due to the unidirectional bending the problem has usually been modeled as two-dimensional. The material considered for this simulation is an aluminum alloy of thickness $t = 0.81$ mm with elastic properties $E = 71$ GPa and $\nu = 0.33$. The plastic behavior is ruled by the Lankford parameters $r_0 = 0.71$, $r_{45} = 0.58$ and $r_{90} = 0.7$ with an isotropic hardening law defined by

$$\sigma_y\left(e^p\right) = 576.79 \times \left(0.01658 + e^p\right)^{0.3593}.$$

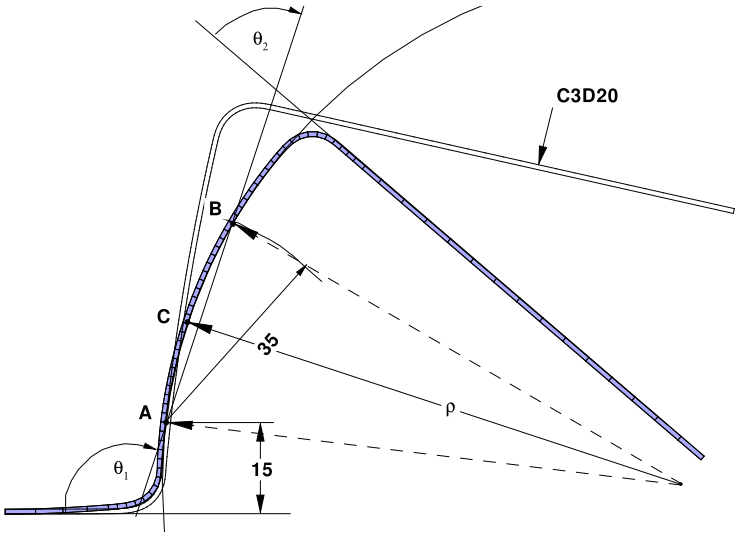

Fig. 14. Elastic springback.

The total blank-holder force is 2.45 kN and a friction coefficient $\mu = 0.162$ has been used for the contact between the blanket and the tools. The simulation consists of two main stages: the U-shaped deep drawing (total punch stroke is 70 mm) and the large displacements elastic springback once the tools are removed.

This example allows to assess the behavior of the element for moderate to large strains ($e^p_{max} < 0.17$) and the remaining elastic state after those deformations. Using symmetry considerations only one quarter of the total geometry is discretized, using 75 elements in longitudinal direction with maximum element size of 5 mm in the parts that are not bent and a minimum element size of 1.5 mm in the parts that slide on the die radii. This element size of 1.5 mm is the maximum allowable to correctly capture the contact due to the small tool radius (5 mm). Larger mesh sizes may lead on one hand to erroneous contact forces and on the other hand to an inaccurate prediction of the elastic springback as discussed in [8]. Ten elements have been used along the half-width. Fig. 14 shows a profile of the blank after the springback stage, where the geometric parameters used to compare with experimental results are indicated. For the present simulation the values obtained were (the values in brackets are the range of experimental results) $\rho = 85.9$ mm [81–99], $\theta_1 = 110.9°$ [110–116] and $\theta_2 = 68.7°$ [68–76]. All the geometric parameters obtained are within the experimental ranges. As in the previous example a comparison with a quadratic standard solid element is included. Fig. 14 also shows the springback profile obtained with code Abaqus/std [30] using one row of the C3D20 solid element (Continuum 3 Dimensional 20-node with full integration). In this case it can be seen that a quadratic standard solid element cannot capture correctly the elastic–plastic bending.

4.10. Deep drawing of a square sheet

The last example considered is the large strain deep drawing of a thin sheet proposed also as a benchmark in Numisheet'93 [39]. Fig. 15 shows details of the tools geometry. The undeformed blanket is square with a side length of 150 mm and thickness $t = 0.78$ mm.

Considering the symmetries along the coordinate axes only one quarter of the geometry has been discretized. A uniform mesh with 60 elements per side (3600 elements) has been used for the blanket and 7 integration points across the thickness. The blank-holder force used is 19.6 kN and the friction coefficient adopted is $\mu = 0.144$. The punch stroke for this deep-drawing is 40 mm. The rather fine mesh considered for this example is to minimize the influence of the in-plane behavior so that the through the thickness behavior may be assessed.

Fig. 16(a) plots the punch forces vs. the punch travel. The figure includes the forces obtained with the classical shell element `BBST` using the same discretization and results obtained with present element and solid element `Solag` using the same in-plane discretization but four element layers across the thickness. Forces obtained with present element using 1 layer and using 4 layers (2 integration points per layer in this case) are in excellent agreement, and are slightly more flexible for the last part of the simulation than those obtained with the fully integrated solid element `Solag`.

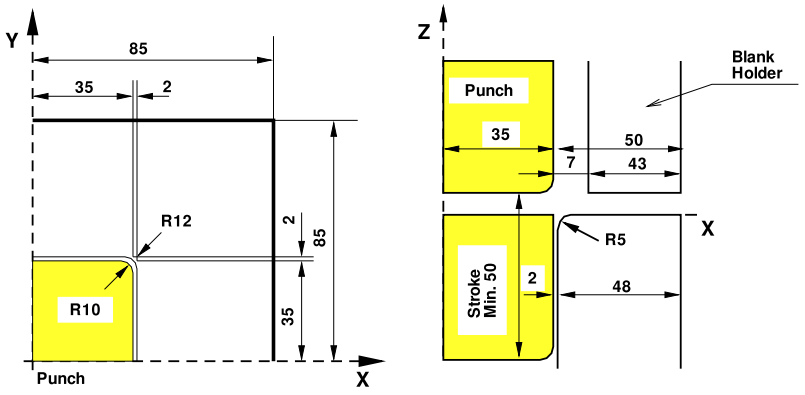

Fig. 15. Deep drawing of square sheet, tool's geometry (dimensions in mm).

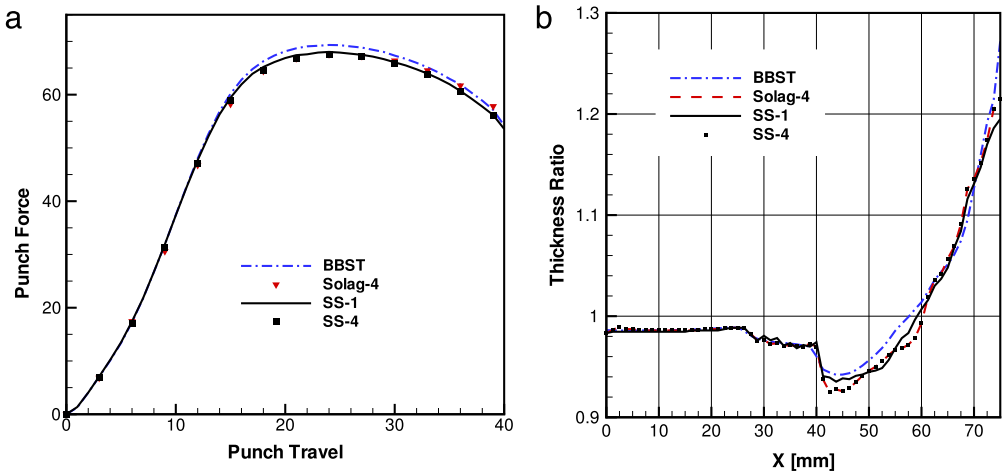

Fig. 16. Deep drawing of a square sheet. (a) Punch force; (b) thickness ratio.

Fig. 16(b) plots the thickness ratio for the maximum punch travel along the symmetry axis x (original distance). In contrast with solid elements, most of the shell elements are not sensitive to equal contact pressures on both surfaces (blank-holder and die). Due to the isochoric plastic flow, the zones with negative in-plane strains lead to larger thickness ratios, and if these points are under the blank-holder they have an important transverse normal stress. In this example this occurs at the mid-side points of the blanket. Clearly the thickness ratio obtained with the shell element is larger than those obtained with solid elements. The results obtained with present element using four layer and the solid element are almost equal.

Finally Fig. 17 plots the equivalent plastic strain contours on the upper surface for a punch travel of 40 mm. Present element results are those in the center of the figure, and for comparison those obtained with solid element `Solag` using 4 layers are shown on the right and with shell element `BBST` on the left. The differences between the three models are mostly quite small.

As reference values Table 2 shows the CPU times necessary for the simulations considered for this benchmark using a code with explicit integration of the equations of motion. The simulations were performed in a PC with an Intel i7-4790 CPU under Windows 7 OS. These values do not allow to draw definitive conclusions due to the large number of aspects involved in the simulations, but they show that the present solid-shell element is a competitive alternative to shell elements for metal forming problems. In a recent paper Bettaieb et al. [40] tested and compared two solid-shell formulation with in-plane reduced and full integration. The tests included sheet metal forming and springback analysis. They concluded that for these problems solid-shell elements are very robust, give excellent results and are quite efficient specially for the reduced integration case.

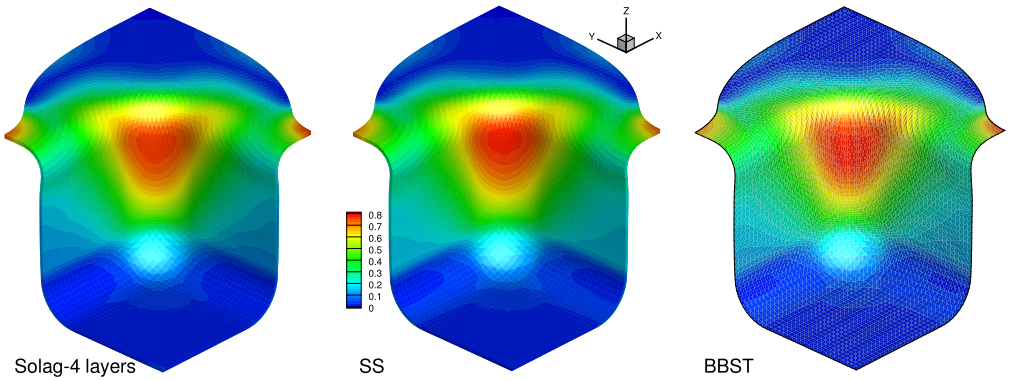

Fig. 17. Equivalent plastic strain for the maximum punch travel.

Table 2
CPU times for the different models.

Model	Elements	Integr. Points	CPU-time [s]	Steps [10^3]
BBST	7 200	7	486	90
Solag-4	14 400	4	2024	118
SS-1	3 600	7	355	50
SS-4	14 400	2	1779	119

5. Conclusions

In this paper an 8-node hexahedral solid-shell element appropriate for the nonlinear elastic–plastic analysis with moderate to large strains has been developed. The Total Lagrangian Formulation used can easily deal with elastic and plastic anisotropy. A mixed assumed strain technique has been used to prevent transverse shear locking and an assumed strain technique to try to improve membrane behavior. To avoid locking due to Poisson effect a modified enhanced assumed strain with one additional degree of freedom has been considered while the volumetric locking is cured resorting to in-plane reduced integration. The sampling points used for the assumed strain techniques are the midpoints of the sides of the upper and lower faces. The right Cauchy–Green tensor computed at those points is interpolated (averaged) at the center of the faces and interpolated along the element thickness. Schemes for cost-efficient stabilization of the membrane and the transverse shear behavior are presented. The formulation is relatively simple and can effectively achieve the objective. The main conclusions are:

- The transverse shear locking disappears completely. Reduced integration avoids volumetric locking in quasi-incompressible problems and the EAS approach prevents locking due to Poisson effect.
- For explicit integration schemes one local iteration for the computation of the internal degree of freedom is enough to obtain accurate results. Even in elastic–plastic problems using the elastic D_{33} leads to good results.
- The results compare very well with results obtained with classical shell elements or shear deformable shell elements. For doubly curved middle surface problems, the element shows excellent convergence properties.
- The element provides correct results in elastic–plastic problems with moderate to large strains.
- The stabilization scheme is relatively simple and computationally inexpensive.
- The value of the stabilization parameter is relevant for coarse meshes only. The same values have be used for the whole range of the numerical examples presented, i.e. it is not necessary to tune the factor for the problem at hand.

Acknowledgments

The author acknowledges financial support from CONICET (Argentina) under grant PIP 11220120100128 and SeCyT-UNC under grant 05/M263.

References

[1] D. Koslov, G. Frazier, Treatment of hourglass patterns in low order finite element codes, Numer. Anal. Methods Geomech. 2 (1978) 57–72.
[2] D. Flanagan, T. Belytschko, A uniform strain hexahedra and quadrilateral and orthogonal hourglass control, Internat. J. Numer. Methods Engrg. 17 (1981) 697–706.
[3] T. Belytschko, W.E. Bachrach, Efficient implementation of quadrilaterals with high coarse-mesh accuracy, Comput. Methods Appl. Mech. Engrg. 54 (1986) 279–301.
[4] T. Belytschko, L.P. Bindeman, Assumed strain stabilization of the eight node hexahedral element, Comput. Methods Appl. Mech. Engrg. 105 (1993) 225–226.
[5] L. Vu-Quoc, J.A. Mora, A class of simple and efficient degenerated shell elements: Analysis of global spurious-mode filtering, Comput. Methods Appl. Mech. Engrg. 74 (1989) 117–175.
[6] L. Vu-Quoc, A perturbation method for dynamic analysis of under-integrated shell elements, Comput. Methods Appl. Mech. Engrg. 79 (1990) 129–172.
[7] F. Abed-Meraim, A. Combescure, An improved assumed strain solid-shell element formulation with physical stabilization for geometric non-linear applications and elastic–plastic stability analysis, Internat. J. Numer. Methods Engrg. 80 (2009) 1640–1686.
[8] B. Bassa, F. Sabourin, M. Brunet, A new nine-node solid-shell finite element using complete 3d constitutive laws, Internat. J. Numer. Methods Engrg. 92 (7) (2013) 589–636.
[9] R.P.R. Cardoso, J.W. Yoon, M. Mahardika, S. Choudhry, R.J. Alves de Sousa, R.A. Fontes Valente, Enhanced assumed strain (eas) and assumed natural strain (ans) methods for one-point quadrature solid-shell elements, Internat. J. Numer. Methods Engrg. 75 (2008) 156–187.
[10] I.B. Edem, P.D. Gosling, One-point quadrature ans solid-shell element based on a displacement variational formulation part i, Comput. Methods Appl. Mech. Engrg. 237–240 (2012) 177–191.
[11] S. Reese, A large deformation solid-shell concept based on reduced integration with hourglass stabilization, Internat. J. Numer. Methods Engrg. 69 (2007) 1671–1716.
[12] M. Schwarze, I.N. Vladimirov, S. Reese, Sheet metal forming and springback simulation by means of a new reduced integration solid-shell finite element technology, Comput. Methods Appl. Mech. Engrg. 200 (2011) 454–476.
[13] M. Schwarze, S. Reese, A reduced integration solid-shell finite element based on the eas and the ans concept—large deformation problems, Internat. J. Numer. Methods Engrg. 85 (2011) 289–329.
[14] V.D. Vuong-Dieu Trinh, F. Abed-Meraim, A. Combescure, A new assumed strain solid-shell formulation “shb6” for the six-node prismatic finite element, J. Mech. Sci. Technol. 25 (2011) 2345–2364.
[15] M. Mostafa, M.V. Sivaselvan, C.A. Felippa, A solid-shell corotational element based on andes, ans and eas for geometrically nonlinear structural analysis, Internat. J. Numer. Methods Engrg. 95 (2013) 145–180.
[16] E.N. Dvorkin, K.J. Bathe, A continuum based four-node shell element for general nonlinear analysis, Eng. Comput. 1 (1984) 77–88.
[17] R. Hauptmann, K. Schweizerhof, A systematic development of solid-shell element formulations for linear and nonlinear analyses employing only displacement degrees of freedom, Internat. J. Numer. Methods Engrg. 42 (1998) 49–70.
[18] J.C. Nagtegaal, D.M. Parks, J.R. Rice, On numerically accurate finite element solutions in the fully plastic range, Comput. Methods Appl. Mech. Engrg. 4 (1974) 153–177.
[19] J.C. Simo, F. Armero, R.L. Taylor, Improved versions of assumed enhanced strain tri-linear elements for 3d finite deformation problems, Comput. Methods Appl. Mech. Engrg. 110 (1993) 359–386.
[20] R. Hautpmann, S. Doll, M. Harnau, K. Schweizerhof, Solid-shell elements with linear and quadratic shape functions at large deformations with nearly incompressible materials, Comput. Struct. 79 (2001) 1671–1685.
[21] L. Vu-Quoc, X.G. Tan, Effcient hybrid-eas solid element for accurate stress prediction in thick laminated beams, plates, and shells, Comput. Methods Appl. Mech. Engrg. 253 (2013) 337–355.
[22] K.Y. Sze, W.K. Chan, A six-node pentagonal assumed natural strain solid-shell element, Finite Elem. Anal. Des. 37 (2001) 639–655.
[23] F.G. Flores, Development of a non-linear triangular prism solid-shell element using ans and eas techniques, Comput. Methods Appl. Mech. Engrg. 266 (2013) 81–97.
[24] O.C. Zienkiewicz, R.L. Taylor, The Finite Element Method, in: Solid Mechanics, vol. II, Butterworth Heinemann, 2000.
[25] F.G. Flores, E. Oñate, Improvements in the membrane behaviour of the three node rotation-free bst shell triangle using an assumed strain approach, Comput. Methods Appl. Mech. Engrg. 194 (2005) 907–932.
[26] F.G. Flores, C.F. Estrada, A rotation free thin shell quadrilateral, Comput. Methods Appl. Mech. Engrg. 196 (2007) 2631–2646.
[27] F.G. Flores, E. Oñate, Un elemento de sólido con una mejora en el comportamiento del corte transversal para el tratamiento de láminas, Rev. Int. Métodos Numér. Cál. Diseño Ing. 27 (4) (2011) 256–268.
[28] F.G. Flores, E. Oñate, A rotation-free shell triangle for the analysis of kinked and branching shells, Internat. J. Numer. Methods Engrg. 69 (2007) 1521–1551.
[29] K.Y. Sze, X.H. Liu, S.H. Lo, Popular benchmark problems for geometric nonlinear analysis of shells, Finite Elem. Anal. Des. 40 (2004) 1551–1569.
[30] ABAQUS/SE. User’s Manual, version 6.9. Dassault Systemes Simulia Corp, 2010.
[31] M. Schwarze, S. Reese, A reduced integration solid-shell finite element based on the eas and the ans concept. geometrically linear problems, Internat. J. Numer. Methods Engrg. 80 (2009) 1322–1355.
[32] U. Andelfinger, E. Ramm, Eas-elements for two-dimensional, three-dimensional, plate and shell structures and their equivalence to hr-elements, Internat. J. Numer. Methods Engrg. 36 (1993) 1311–1337.
[33] E.P. Kasper, R.L. Taylor, A mixed-enhanced strain method part i: geometrically linear problems, Comput. Struct. 75 (2000) 237–250.
[34] S. Klinkel, F. Gruttmann, W. Wagner, A robust nonlinear solid shell element based on a mixed variational formulation, Comput. Methods Appl. Mech. Engrg. 195 (2006) 179–201.

[35] L. Vu-Quoc, X.G. Tan, Optimal solid shells for non-linear analyses of multilayer composites. i. Statics, Comput. Methods Appl. Mech. Engrg. 192 (2003) 975–1016.
[36] J.C. Simo, D.D. Fox, M.S. Rifai, On a stress resultant geometrically exact shell model. Part iii: Computational aspects of the non-linear theory, Comput. Methods Appl. Mech. Engrg. 79 (1990) 21–70.
[37] S. Glaser, F. Armero, On the formulation of enhanced strain finite element methods in finite deformations, Eng. Comput. 14 (7) (1997) 759–791.
[38] E.A. Souza Neto, F.M. Andrade Pires, D.R.J. Owen, F-bar-based linear triangles and tetrahedra for finite strain analysis of nearly incompressible solids. Part i: Formulation and benchmarking, Internat. J. Numer. Methods Engrg. 62 (2005) 353–383.
[39] A. Makinouchi, E. Nakamachi, E. Oñate, R. Wagoner, Proceedings of the International Conference NUMISHEET'93, 1993.
[40] A. Ben Bettaieb, J.L. Velosa de Sena, R.J. Alves de Sousa, R.A.F. Valente, A.M. Habraken, L. Duchêne, On the comparison of two solid-shell formulations based on in-plane reduced and full integration schemes in linear and non-linear applications, Finite Elem. Anal. Des. 107 (2015) 44–59.